

# Time-dependent spectral-feature variations of stars displaying the B[e] phenomenon ★ ★★

## III. HD 50138

T. Jeřábková<sup>1,4</sup>, D. Korčáková<sup>1</sup>, A. Miroshnichenko<sup>2</sup>, S. Danford<sup>2</sup>, S. V. Zharikov<sup>3</sup>, R. Křiček<sup>1</sup>, P. Zasche<sup>1</sup>, V. Votruba<sup>4,5</sup>, M. Šlechta<sup>4</sup>, P. Škoda<sup>4</sup>, and J. Janík<sup>5</sup>

<sup>1</sup> Astronomical Institute, Charles University in Prague, V Holešovičkách 2, CZ-180 00 Praha 8, Czech Republic

<sup>2</sup> Department of Physics and Astronomy, University of North Carolina at Greensboro, Greensboro, NC 27402, USA

<sup>3</sup> Instituto de Astronomía, Universidad Nacional Autónoma de México, Apartado Postal 877, 22830, Ensenada, Baja California, México

<sup>4</sup> Astronomical Institute of the Academy of Science of the Czech Republic, Fričova 298, CZ-251 65 Ondřejov, Czech Republic

<sup>5</sup> Institute of Theoretical Physics and Astrophysics, Masaryk University, CZ-611 37 Brno, Kotlářská 2, Czech Republic

Received 10 May 2015; accepted 6 November 2015

### ABSTRACT

**Context.** B[e] stars are anomalous objects around which extended circumstellar matter is present. The observed properties of the central star are significantly affected by the surrounding material. Therefore, the use of standard synthetic spectra is disputable in this case and our capability to study these objects is limited. One of the possibilities is to analyse variations of the spectral features. Long-term spectroscopic observations are required for this, but are not found in the literature.

For our study we choose the B[e] star HD 50138 of the FS CMa type because of the indication that this star is a post-main-sequence star, although still not highly evolved. Therefore, it can be a good object for testing evolutionary models. Currently, HD 50138 is the most extensively observed FS CMa star which makes it an ideal object for modelling. Our observations fill the gap in the available data.

**Aims.** To describe the variability of HD 50138 we have monitored this star spectroscopically over the last twenty years. To search for the periodicity on short-term scales, series of night-to-night observations were also obtained. We were able to obtain 130 spectra from four different telescopes – 1.06 m at Ritter Observatory (échelle,  $R \sim 26\,000$ , 32 spectra, 1994 – 2003), the Perek 2 m telescope at Ondřejov Observatory (slit,  $R \sim 12\,500$ , 56 spectra, 2004 – 2013), the 2.12 m telescope at Observatorio Astronómico Nacional San Pedro Martir (échelle,  $R \sim 18\,000$ , 16 spectra, 2005 – 2013), and the 0.81 m telescope at Three College Observatory (échelle,  $R \sim 12\,000$ , 26 spectra, 2013 – 2014).

**Methods.** We describe and analyse variations of the chosen lines. The measurements of the equivalent widths and radial velocities of the  $H\alpha$ ,  $H\beta$ , and  $[O\text{I}] \lambda\lambda 6300, 6364 \text{ \AA}$  lines are presented. The set of obtained spectra allows us to describe the changes on timescales from days to years.

**Results.** The long-term quasi-periodic trend was found in the variations of the  $H\alpha$  equivalent width and confirmed by time dependent studies of the relative flux and equivalent width of the  $[O\text{I}] 6300 \text{ \AA}$  line and radial velocity of the  $H\alpha$  violet peak. The two long periods of  $3\,000 \pm 500$  and  $5\,000 \pm 1\,000$  days were detected there. We were able to catch moving humps in the  $H\alpha$  line, which reveal the rotating media around the star. An analysis of the correlation of equivalent widths, radial velocities, relative fluxes, and  $V/R$  ratios for various lines is presented in detail.

**Conclusions.** We describe the spectral variability of HD 50138 over the last twenty years. Based on these data, we determine new restrictions for future modelling. We confirm the quasi-periodic behaviour of the object's spectral variability, which probably reflects mass transfer in a binary system. This behaviour also supports a recently introduced explanation of the nature of FS CMa stars as post-merger systems.

**Key words.** circumstellar matter – stars: emission line, Be – stars: mass loss – binaries: spectroscopic – stars: individual: MWC 158

## 1. Introduction

The B[e] phenomenon (IAUS 70, Conti 1976) is a designation for hot B-type stars whose spectra show forbidden and permitted emission lines of neutral and singly ionised atoms and strong infrared excess (Swings & Allen 1971). These observed properties indicate very extended circumstellar matter and were discovered

in only a small percentage of known B stars. However, stars of different types and in different evolutionary stages show the B[e] phenomenon. Lamers et al. (1998) were able to identify compact planetary nebulae, Herbig stars, supergiants, and symbiotic stars, but they were not able to classify half of the stars known at that time. Miroshnichenko (2007) noticed that almost all unclassified stars have similar properties and introduced a new group called FS CMa objects. To date, the nature of FS CMa stars has not yet been explained. The amount of dust is too large to be produced during the evolution of a single star. One likely explanation is

\* Based on data from Perek 2 m telescope, Ondřejov, Czech Republic.

\*\* Figs. 1–4, 6, 8, 10–12, 14–16, 21, 22, 26, 28, 29 and Tables 2 – 10 are available in electronic form at [www.aanda.org](http://www.aanda.org).

that these are binary stars, but a sufficient number of binaries have not been identified in this group. Detailed discussion of the nature of FS CMa stars can be found in Miroshnichenko (2007); Miroshnichenko et al. (2013), and Miroshnichenko & Zharikov (2015).

The study of FS CMa stars is complicated by the presence of large amounts of circumstellar matter. We usually have almost no direct information about the central object. Moreover, due to asymmetry of the envelope and its large extension, commonly used stellar atmosphere models are not appropriate for the analysis. Therefore, in the present study we focus on spectral variability which provides one of only a few limited opportunities to study these objects. Despite the importance of these observations, long-term monitoring data are still missing for most group objects. The first two papers (Polster et al. 2012; Kučerová et al. 2013) were devoted to systematic spectroscopic observations of the FS CMa objects MWC 623 and MWC 342. Here we present the results of a spectroscopic monitoring of HD 50138, the brightest star of the FS CMa type.

HD 50138 (MWC 158, V743 Mon, or IRAS 06491-0654) was discovered to be an emission-line star by Humason & Merrill (1921) on a photographic plate from December 1920. Soon afterwards, Merrill et al. (1925) noticed its spectral variability. Following this discovery Merrill (1931) published the results from almost ten years of spectroscopic observations. He analysed 76 photographic plates obtained from December 1920 to February 1930 (mostly in the blue region around the  $H\beta$  line). The radial velocity ( $RV$ ) measurements indicated a period of about 30 days. However, this period did not fit the measurements well. An attempt to fit with two periods or variable elements of a binary also failed owing to insufficient data sampling. Another systematic study was done by Doazan (1965). She analysed 52 spectra ( $12.4 \text{ \AA/mm}$ ) from the Haute Provence observatory obtained between 1960 and 1963. She found that the envelope was expanding continuously. Moreover, the speed of expansion was changing periodically on timescales of 50 days. The acceleration of matter was observed during a half cycle and was followed by its deceleration in the following half cycle. A detailed spectroscopic study was published by Jaschek & Andrillat (1998). Spectra in the interval from  $3738 - 10232 \text{ \AA}$  (dispersion  $33 \text{ \AA/mm}$ ) obtained in 1989 and 1996 at the Haute Provence observatory allowed them to determine basic properties of the envelope. However, the set of 22 spectra in nine different intervals did not permit a sufficient description of the variability. Another attempt (and the last so far) to find the spectral periodicity was made by Corporon & Lagrange (1999). They measured  $RV$ s on high-dispersion spectra ( $R = 50000$ ) obtained during a three-year campaign started in 1994. They found no trend. However, they used an automatic fitting to a Gaussian profile to measure the  $RV$ . Since the chosen absorption lines are asymmetric and variable, this procedure may be questioned. Other studies are based on only a few spectra or on a short campaign prohibiting detection of variability of this source.

The star is also photometrically variable, but the amplitude of changes is small, no greater than a tenth of a magnitude. HD 50138 as a variable star was first noted by Allen (1973) based on observations in the IR region from February 1971 to January 1972. Ultraviolet observations from 1974 and 1975 were analysed by Savage et al. (1978). They found that the changes are wavelength dependent and the largest change was detected at  $0.25 \text{ \mu m}$ . Observations in the Johnson photometric system have been done by Alvarez & Schuster (1981). They found no vari-

ability, but their analysis was only based on five measurements. More systematic work was done by Kilkenny et al. (1985). They obtained photoelectric measurements (UBVRIY) from March 1981 to April 1982 and detected variations of the order of 0.09 mag. The magnitude of variations probably differs between the observation epochs (as in another B[e] star – V1972 Cyg; Mel'nikov (1997)), which is indicated by the observations performed by de Winter et al. (2001). Unfortunately, the observations are too sparse to find periodicity, multiperiodicity, or other regular behaviour of this star.

HD 50138 is variable not only spectroscopically and photometrically, but also polarimetrically. Different results have been presented by e.g. Bjorkman & Schulte-Ladbeck (1994) and Yudin & Evans (1998). Data from Bjorkman & Schulte-Ladbeck (1994) can be explained by a rotating dusty disc, or binarity of the object. Further polarimetric observations (Bjorkman et al. 1998) have allowed a picture to be constructed of the circumstellar matter: a thin gaseous disc, viewed almost edge-on, together with an optically-thin spherically symmetric dusty shell. Detailed polarisation measurements along the  $H\alpha$  line (Harrington & Kuhn 2007) show changes in the polarisation in the absorption part of the line. This leads Harrington & Kuhn (2007) to suggest that optical pumping (rather than scattering) plays an important role in the envelope.

Another technique that gives important information about the circumstellar material is interferometry. The first interferometric measurements at  $10.7 \text{ \mu m}$  were obtained in 2005 by Monnier et al. (2009) using the Keck telescope. The fit of the visibility by a 1D Gaussian function gives a size estimate of  $58 \pm 6 \text{ mas}$ ; a 2D Gaussian gives  $(66 \pm 4) \times (46 \pm 9) \text{ mas}$  with a position angle  $63 \pm 6 \text{ deg}$ . Further observations using the MIDI and AMBER instruments at VLTI allowed the study of the dependence of the size of the circumstellar matter on the wavelength (Borges Fernandes 2010; Borges Fernandes et al. 2011). Recently Ellerbroek et al. (2015) has published results from the VLTI/AMBER and CHARA/VEGA interferometer completed by the VLT/CRIRES spectro-astrometry and other spectroscopic and spectropolarimetric data. They found that the  $\text{Br}\gamma$  emission originates in a compact region up to 3 au and the continuum emission is produced in a more extended region. They also proved that Keplerian rotation dominates the velocity field. Marston & McCollum (2008) attempted to find signatures of more extended media using CCD images taken through a narrow  $H\alpha$  filter with a 60-inch telescope. They detected no nebula.

The circumstellar matter of HD 50138 was modelled first using the Sobolev approximation by Doazan (1965) and Briot (1981). Kuan & Kuhi (1975) derived the mass loss rate by this method for the first time. The conditions in the envelope suggest the use of a model involving the Strömgren sphere (Houziaux & Andrillat 1976). A more detailed model using the Monte Carlo method was published by Bjorkman et al. (1998).

In recent years several events have been observed leading to the formation of a new shell (Hutsemekers 1985; Pogodin 1997). The announcement from Andrillat & Houziaux (1991) was followed by photometric (Halbedel 1991) and spectroscopic (Bopp 1993) observations.

The detection of such events, or of corotating regions in the circumstellar disc, as well as the confirmation of the binary nature of the system, can be done within the framework of our project. Binarity is one of the current key hypotheses regarding stars of the FS CMa type. The amount of circumstellar matter in these objects is larger than predicted by the evolutionary mod-

**Table 1.** Parameters of the spectrographs used.

	Ondřejov O.	Ritter O.	SMP O.	TCO
R ( $H\alpha$ ) $\approx$	12 500	26 000	18 000	12 000
spectr.	slit	échelle	échelle	échelle
PMD [m]	2.0	1.06	2.12	0.81
notation	OO ●	RO *	SMP ▲	TCO +

**Notes.** The resolution, type of the spectrograph, and diameter of the primary mirror are summarised. The last row introduces the notation to be used, which corresponds to the individual instruments.

els of single stars, but only 30% of them have been proved or suggested to be binary systems (Miroshnichenko 2007).

In Sect. 2 we describe the observations and the data reduction process. The line-profile variability, measurements of the equivalent widths ( $EW$ s), and  $RV$ s are presented in Sects. 3 and 4. The observed phenomenon are discussed in detail in Sect. 5. Conclusions are presented in Sect. 6.

## 2. Observations and data reduction

Our analysis is based on data from several observatories. The main properties of the equipment used are summarised in Table 1. The main data set presented here was taken during years 2004–2013 with the Perek 2 m telescope at Ondřejov Observatory (OO), Czech Republic. For our observations we chose a spectral interval from 6265 Å to 6770 Å because of a) the presence of the forbidden emission lines [O I]  $\lambda\lambda$  6300, 6364 Å, which are formed in the outer parts of the envelope; b) the Si II  $\lambda\lambda$  6347, 6371 Å, and He I 6678 Å lines, which originate in the inner parts; and c) the  $H\alpha$  line, which forms over a wide range of distances from the star. Therefore, starlight can be affected by a wide range of phenomena as it passes through the entire envelope.

The data<sup>1</sup> are reduced in IRAF<sup>2</sup> using standard procedures. To remove cosmic rays, the program dcr (Pych 2004) is used. This allows us to omit the use of the optimal extraction during the spectra subtraction. Considering that our spectra are parallel to the pixel rows, their subtraction is possible by individual pixel columns. Therefore, atmospheric night sky lines do not affect the stellar forbidden oxygen lines<sup>3</sup>. Because of the high intensity of the  $H\alpha$  line, which is almost twenty times higher than the continuum, normalisation is an important step in the reduction process. Fortunately, the continuum in the interval around the  $H\alpha$  line is well defined, which provides a good fit by Chebyshev polynomials. To check the accuracy of the normalisation, we changed the order of the polynomial ( $\pm 1$ ) and the chosen continuum intervals. The resulting values ( $EW$ s, relative fluxes, and  $RV$ s) differ within their error estimates.

Another set of spectra were taken in 1993–2005 at the Ritter observatory (RO), Toledo, Ohio. These échelle spectra were reduced using standard IRAF and IDL routines. The normalisation of individual échelle orders was similar to the Ondřejov data. We decrease the RO spectral resolution to the Ondřejov value using convolution by a Gaussian function.

We also used spectra from Observatorio Astronomico Nacional San Pedro Martir (SPM). Spectra were reduced using the standard procedures in IRAF without the optimal extraction. The construction of the spectrograph and reduction process guarantee that the final spectrum is not affected by the night-sky lines. MIDAS was used to clean spectra from cosmic rays.

The last set of spectra are from Three College Observatory (TCO, located near Greensboro, North Carolina, USA). All the TCO data were reduced using IRAF, specifically its échelle package to extract the spectral orders, identify lines in the comparison ThAr spectra, and complete the wavelength calibration of the objects' spectra.

Time intervals between individual observations were very different across the series. Sequential spectra were obtained on several nights, as well as the night-to-night series. On the other hand, the intervals between some observations exceeded a month in some seasons. Detailed coverage of observations was achieved in the last season when the average temporal step was five days. This data set allowed us to find or reject periods in the range from a few days to years. The list of observations is printed in Table 2<sup>e</sup>4.

## 3. Analysis

To describe the observed changes of the spectral lines, we measure their  $EW$ s,  $RV$ s, and relative fluxes. We summarise the procedures used in this section because of the specification of the error estimate, which is as important as the value itself for the rigorous analysis of temporal variability.

- i)  $EW$  measurements using line-profile integration:  
Numerical integration by the trapezium method is used on the interpolated data (Steffen 1990). Errors are estimated according to Vollmann & Eversberg (2006) where the signal-to-noise ratio ( $S/N$ ) is taken into account. The value of  $S/N$  is estimated by a linear fit of the appropriate part of the continuum. This straightforward integration is used for the  $H\alpha$  line.
- ii)  $EW$  determined by fitting of a Gaussian function:  
Narrow symmetric lines ([O I]  $\lambda\lambda$  6300 Å, 6364 Å) are fitted by a Gaussian function. The least squares method is used for the procedure and the error estimate is calculated following Vollmann & Eversberg (2006).
- iii)  $RV$  and line intensities obtained by Gaussian fitting:  
The procedure is identical to the one described in item ii), except for the error estimate, which is determined by both the formal error of the least squares method and Monte Carlo simulation based on the  $S/N$ .
- iv) polynomial fitting:  
 $RV$ , line intensities, or extrema of several functions are fitted by a polynomial (3<sup>rd</sup>–6<sup>th</sup> order) using the least squares method. The error is a formal error of this method combined with the error estimated from the  $S/N$  using the Monte Carlo method.
- v)  $RV$  determined by the line-profile mirroring:  
The flipped line is shifted automatically using the least squares method to fit the chosen part of the line (Fig. 1<sup>e</sup>). The uncertainty is computed as a combination of the error of the fit and the  $S/N$  ratio.
- vi) period analysis:  
We use a Scargle periodogram analysis code written by

<sup>1</sup> Continuum normalised spectra are available at the CDS database.

<sup>2</sup> IRAF is distributed by the National Optical Astronomy Observatories, operated by the Association of Universities for Research in Astronomy, Inc., under contract to the National Science Foundation of the United States.

<sup>3</sup> The spectrum obtained on 7 February 2005 was reduced by MS using optimal extraction.

<sup>4</sup> Throughout the paper the online material is indicated by the superscript <sup>e</sup>.



K. Bjorkman, which is based on the Fourier transformation for data that are not equally spaced using the Lomb-Scargle method (Press & Teukolsky 1988). All the significant peaks are then independently checked by the code HEC27<sup>5</sup>, written by Petr Harmanec, based on Stellingwerf's method (Stellingwerf 1978).

## 4. Results

We discuss the observed line-profile variations and present *RV* and *EW* measurements for the  $H\alpha$ ,  $H\beta$ , and  $[O\text{I}]$  lines. We did not measure *RV*s and *EW*s of  $\text{Fe II}$ ,  $\text{Si II}$ , and  $\text{He I}$ . The  $\text{Fe II}$  lines are too faint to be measured. The  $\text{Si II}$  and  $\text{He I}$  lines have a complicated structure; therefore, neither *EW* nor *RV* have any clear physical meaning.

To show temporal variability in the chosen spectral lines we use the grey-scale representation. Spectra are rearranged in wavelengths by interpolation (Steffen 1990) and plotted chronologically in a row. The value of relative flux is shown by the shades. We plot relative fluxes  $F$  (dynamical spectra), variance  $\left(\frac{F-\bar{F}}{\bar{F}}\right)$ , and absolute variance  $\left(\frac{F-\bar{F}}{\bar{F}}\right)$  from the mean relative flux  $\bar{F} = \frac{\sum_{i=1,n} F_i}{\sum_{i=1,n} 1}$ , where  $n$  is the number of observations. We show the dynamical spectra in the printer version of this paper, while the other figures are only shown in the electronic version.

### 4.1. Line identification

To identify spectral lines, we use the previous identification done by Doazan (1965) and the NIST<sup>6</sup> database. The spectrum of HD 50138 in the chosen interval contains both emission and absorption lines, forbidden emission lines of neutral oxygen  $[O\text{I}]$   $\lambda\lambda$  6300, 6364 Å, and weak emission lines of permitted singly ionised iron lines  $\text{Fe II}$   $\lambda\lambda$  6318, 6384 Å. The chosen spectral region together with the identification is shown in Fig. 2<sup>e</sup>.

### 4.2. $H\alpha$ line

The  $H\alpha$  line is the most intense line in the spectrum of HD 50138. Though one might expect this to be an advantage, it was not in this case. It was very difficult to obtain good-quality spectra with photographic plates, and the high-resolution échelle spectra usually do not cover enough of the surrounding continuum to normalise it. Moreover, the  $H\alpha$  line forms in an extensive part of the circumstellar medium and hence reflects a broad range of physical conditions. Analysis of this line is very complicated, especially in the extended inhomogeneous circumstellar environments that exist around B[e] stars. Recently, numerical models became available for the analysis. It is possible to use a combination of multidimensional radiative transfer codes (Zsargó et al. 2008; Carciofi & Bjorkman 2006, 2008; Korčáková & Kubát 2005) with multidimensional (Curé 2004) and time-dependent (Votruba et al. 2007) hydrodynamics. The situation is particularly complicated in the case of HD 50138. The polarimetric measurements of Oudmaijer & Drew (1999) show that there must be two distinct line-forming regions for the  $H\alpha$  line. They found that the red peak shows strong depolarisation, the violet peak only slight depolarisation, but the polarised

fluxes are almost equal. They explain this behaviour as a rotating disc located close to the star and a single-peaked emission originating in an extended region.

The  $H\alpha$  line variations can give important supplementary information for the construction of a realistic model in the future. Therefore, we present here our observations, and also summarise the measurements from previous studies (Tables 3<sup>e</sup>, 4<sup>e</sup>, 5<sup>e</sup>, and 6<sup>e</sup>).

#### 4.2.1. $H\alpha$ line-profile variations

Since the discovery of HD 50138 as an emission-line star in 1920, the  $H\alpha$  line has always been observed to be very intense and double peaked (see Fig. 4<sup>e</sup>). The violet peak was smaller than the red peak in all previous studies (Table 3<sup>e</sup>). However, we measured the flux ratio of the violet and red peaks ( $V/R$ , Fig. 7, bottom panel) to exceed 1.0 in two spectra (4 and 10 October 2008 at SPM).

The profile of the violet peak is more complicated than the red one. Moving humps were often detected in high-resolution data, sometimes so strong that it can be called peak splitting (Dachs et al. 1992, Fig. 6; our observations on 6 and 16 February 1994, RO, and 10 November 2007, SPM). Our data sample is sufficiently rich to be able to describe the behaviour of the moving humps (Figs. 5 and 6<sup>e</sup>) and measure their *RV*s (Fig. 9, lowermost panel). This could be a good tracer of the circumstellar environment, e.g. the rotation or expansion of the matter. The humps were also detected in the red peak; however, their appearance is very rare. We were able to capture it at the high-resolution data from the RO on 11 and 21 September 1994, and several times it appeared only as a small deformation of the red peak in data sets from every observatory.

Very important is the detection of a small emission peak in the central absorption (Fig. 3<sup>e</sup>), which could be a signature of the binarity of the object. This emission can originate near the Lagrangian point L1 and hence appears at the zero velocity of the system. It has only been observed once before, on 22 March 1991 (Bopp 1993). We were able to catch it at seven spectra from RO (22/12/1994, 9/2/1998, 15/2/1998, 30/3/1998, 6/4/1998, 13/4/1998, 6/3/2000), and three spectra from TCO (10/12/2013, 15/12/2013, and 26/12/2013). The spectra taken on 15 February 1998, 30 March 1998 exclude possible contamination by the water absorption.

The  $H\alpha$  line is strongly variable. Both night-to-night changes as well as long-term changes have been mentioned in the literature many times. The complex study of night-to-night variations is presented in Pogodin (1997). He analysed 71 spectra obtained from 15 to 18 March 1994. The amplitude of *EW* changes is up to 15%. The residuals of the line profiles, tracing important features of the circumstellar matter, are based on a few average spectra from each night. This observation strategy is able to reveal the variations on the timescale of hours; however, no note is mentioned there. In order to describe the variability on timescales from hours up to years, we acquired sequential spectra during one night, and several following nights on a number of different occasions. The  $H\alpha$  line profiles from one such run (March 2007, OO) is plotted in Fig. 4<sup>e</sup>. We found that the changes in the  $H\alpha$  line during one night are negligible. This allows us to study the long-term variability, which to date has not been described.

<sup>5</sup> <http://astro.troja.mff.cuni.cz/ftp/hec/HEC27/>

<sup>6</sup> P.J. Linstrom and W.G. Mallard, Eds., NIST Chemistry WebBook, NIST Standard Reference Database Number 69, National Institute of Standards and Technology, Gaithersburg MD, 20899, <http://webbook.nist.gov>, (retrieved 12 June 2014)

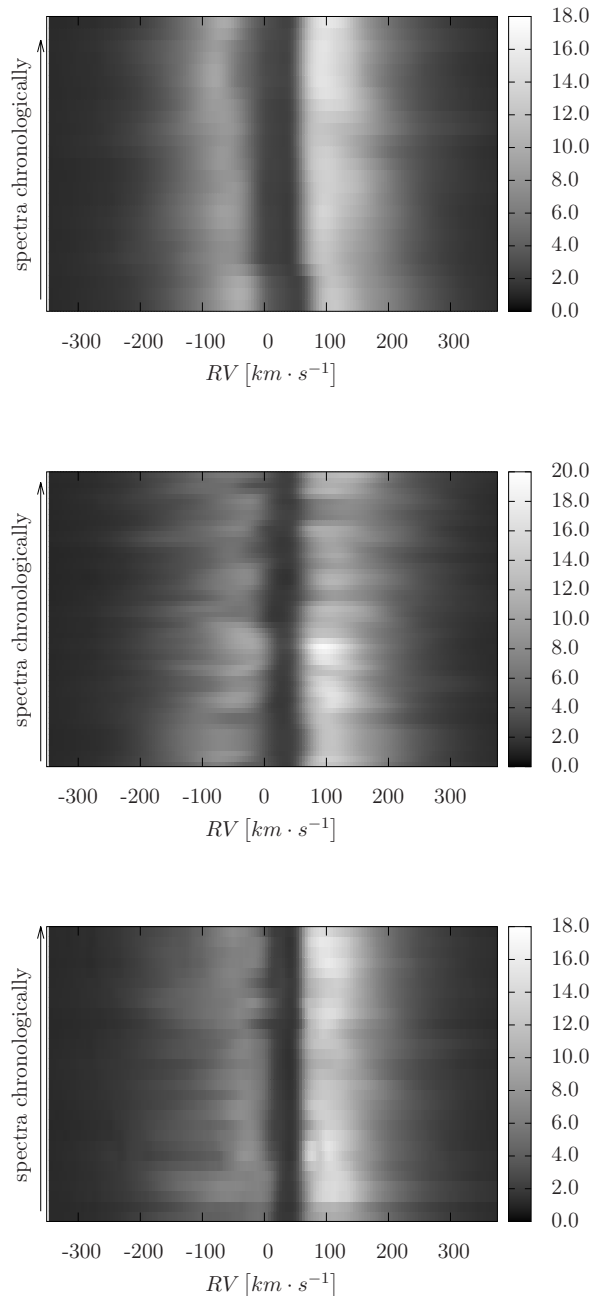


**Fig. 5.** Grey-scale representation of the H $\alpha$  line. Top: spectra from TCO, Middle: spectra from OO, Bottom: spectra from RO.

#### 4.2.2. Relative fluxes, $V/R$ ratio

To describe the variations of the H $\alpha$  line, we measure the intensity of both of the peaks and of the central depression. The values obtained by the polynomial fitting (Sect. 3, *iv*) are presented in Fig. 8<sup>e</sup>. The ratio of the violet and red peak is plotted in the bottom panel of Fig. 7. To see the variability on longer timescales than our observations, we summarise all the measurements presented in the previous works in Table 3<sup>e</sup>. Even if the  $V/R$  ratio does not conserve with respect to different resolutions for asymmetric lines, it can be used for the rough guess of the variability. The values of  $V/R$  were observed in the interval from

0.36 (Borges Fernandes et al. 2009) up to 1.21 (our data, Fig. 7, 4 October 2008). The violet peak was always smaller the red one, with the exception of a short period in October 2008 caught in our spectra.

#### 4.2.3. Equivalent width

We measure the  $EW$  of the H $\alpha$  line by numerical integration (Sect. 3, *i*). Results of our measurements are plotted in Fig. 7. The maximum value (minimum line strength)  $-29.74 \pm 1.54 \text{ \AA}$  is obtained on 6 February 1994. The minimum value (maximum line strength) in our data  $-78.96 \pm 1.65 \text{ \AA}$  corresponds to 13 March 2007. The previous observations, summarised in Table 4<sup>e</sup>, are in the interval defined by these limits with only one exception; the first measurement on 20 February 1960 (Doazan 1965). The  $EW$  at the beginning of the 1960s was  $-116 \text{ \AA}$ . Unfortunately, we can find no published data for more than twenty years following the 1960s. We can only guess that the variability of the object is greater than is shown in our spectra.

#### 4.2.4. Radial velocities

The  $RV$  of both peaks (Fig. 9, top two panels) and central depression (Fig. 9, central panel) of the H $\alpha$  line is estimated by the least squares fitting of the polynomial (Sect. 3, *iv*). The hump in the blue peak of the H $\alpha$  line was strong enough in some spectra to be measured. The sampling of measurements is sufficiently fine to reveal the motion of the humps for two epochs, where the  $RV$  of the humps (Fig. 9, lowermost panel) can be fit by a parabolic function (blue lines in this figure). This shape indicates the rotation motion of the humps more than the pure expansion, which will follow a linear dependence. The wings of the H $\alpha$  line are measured using the mirror method in the relative flux between values 1.05 and 1.4 (Sect. 3, *v*). The results are plotted in Fig. 9 (fourth panel).

The  $RV$  of the central depression, peaks, and wings from previous studies are listed in Table 5<sup>e</sup>. However, the comparison of measurements is not straightforward. The position of the H $\alpha$  line extremum depends on the resolution because the shapes of the peaks and especially the central depression are not symmetric.

#### 4.2.5. Correlation between individual quantities of the H $\alpha$ line

The changes of the observed profile of the H $\alpha$  line are displayed in Figs. 5 – 9. However, because of the different temporal steps between individual observations, it is possible that some important dependencies between quantities may be suppressed in these diagrams. Therefore, we present the most significant values of the Pearson coefficient in Table 7<sup>e</sup>. The most important dependencies are the following:

- i) the correlation between fluxes and the absolute value of  $EW$ ;
- ii) the correlation of peak fluxes themselves, and the flux of the violet peak and the central depression (Fig. 10<sup>e</sup>);
- iii) the strong correlation between  $RV$ s of peaks and the central depression (Fig. 11<sup>e</sup>);
- iv) the  $RV$ s of the wings and the violet peak. These have an almost limited value of the Pearson coefficient (0.13), which prevents the use of this quantity for the determination of the role of the wind or binarity;
- v) the connection between the  $EW$  and  $RV$ s (Fig. 12<sup>e</sup>);
- vi) the lack of dependence between the  $RV$  of wings and peak  $RV$ s and fluxes.

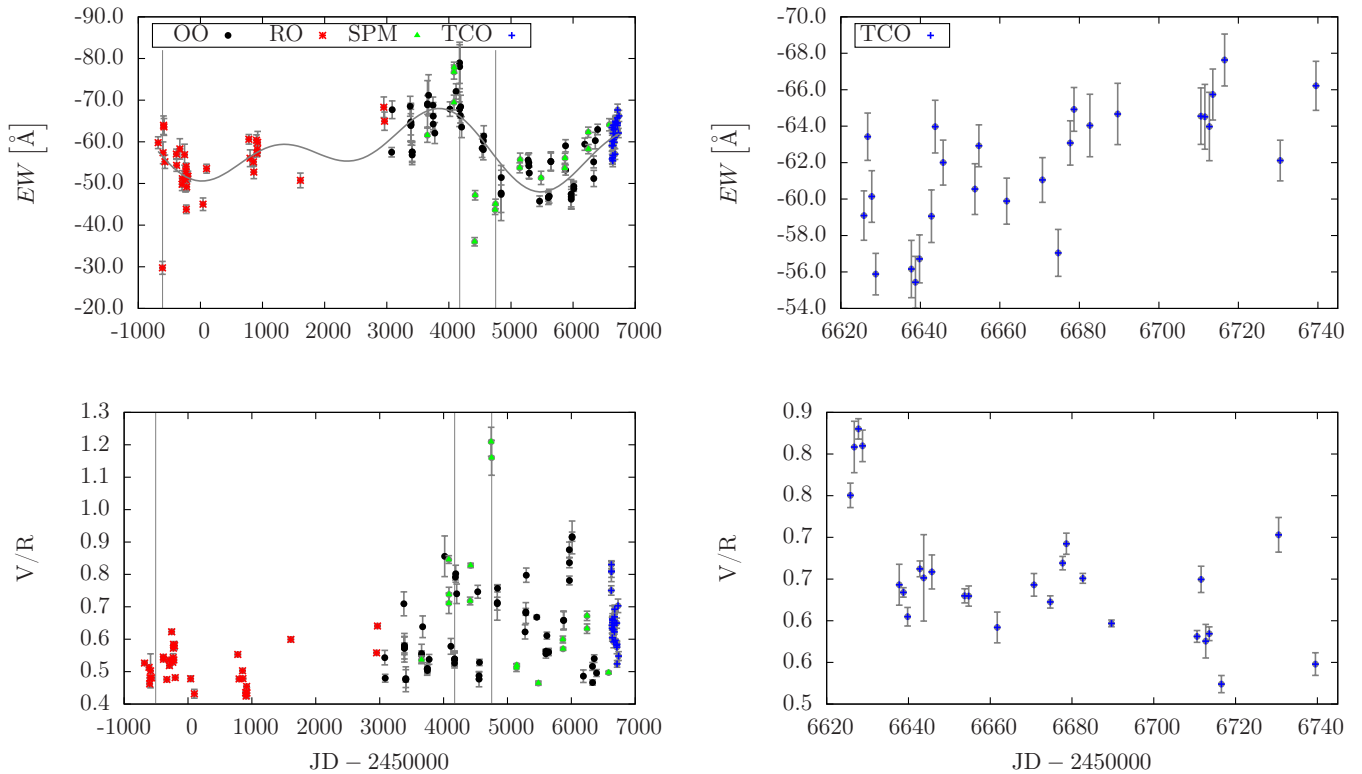


**Fig. 7.** *EW* and *V/R* ratio of relative fluxes of the  $H\alpha$  line. Vertical lines indicate the minimum and maximum values of  $|EW|$  ( $JD = 2\,449\,389.68$ , and  $2\,454\,174.28$ ), and time when  $V/R > 1$  ( $JD = 2\,454\,752.92$ ), respectively.

We note that the interpretation of the Pearson coefficient is not always straightforward in this star. The situation is complicated here by the episodic gas discharge (Sec. 5.4), which can distort the observed dependencies during some epochs. This was recognised in several correlation diagrams, particularly in dependencies between the *RV* of the  $H\alpha$  red peak and the flux of the violet peak, and the *RV* and flux of the central depression. Based on these values, we were able to identify four epochs (Table 7<sup>e</sup>) in which the behaviour of the  $H\alpha$  line was substantially different: prior to  $JD\,2452110$ ,  $2452110 - 2454650$ ,  $2454650 - 2456600$ , and subsequent to  $JD\,2456600$ . Moreover, this classification matches epochs identified in the *RV* of the central depression and *V/R* ratio. These four epochs are seen in data from all four observatories in the present study.

### 4.3. $H\beta$ line

The  $H\beta$  line shows a more complicated behaviour than the  $H\alpha$  line. It had always been observed as an absorption line overlapped by two emission peaks. During the ten-year systematic study of Merrill (1931) in 1920s the red peak remained almost constant, while the violet peak showed large changes. Miczaika (1950) reported observations on 29 January 1949 when the violet part of the line almost disappeared. Another three-year systematic study presented by Doazan (1965) in the 1960s shows a strong variability of both peaks.

The structure of the  $H\beta$  line is often complicated by the presence of moving humps (e.g. Doazan 1965). The size of the humps, relative to the line itself, is greater than is observed in the  $H\alpha$  line. This allows easier detection of the humps and makes the  $H\beta$  line a good tracer of the structure of the material close to the central object where the line is forming.

We present here measurements of the basic parameters of the  $H\beta$  line, excluding the *EW*. The *EW* is not measured because the central depression is below the continuum, and therefore the value of the *EW* has no explicit physical meaning.

#### 4.3.1. Relative fluxes and radial velocities

We measure the relative fluxes and *RV* of both of the peaks and central depression using a least squares polynomial fit (Sect. 3, *iv*). The *V/R* variations and the relative flux of the central depression are plotted in Fig. 13. The relative fluxes of the peaks themselves are presented in Fig. 14<sup>e</sup>. The results of *RV* measurements are plotted in Fig. 15<sup>e</sup>.

#### 4.3.2. Correlation between $H\beta$ and $H\alpha$ lines

The correlation between the  $H\beta$  and  $H\alpha$  lines can be investigated only on the data from the SPM and TCO observatories. This data set shows no strong correlation. However, the maximum of the *RV* of the central depression occurs between these two data samples (see Sect. 4.4.1). Therefore, we also analysed the data from TCO separately. Even if the sample is too small (critical value of  $P = 0.37$ ), strong dependent relationships between several measured quantities (Fig. 16<sup>e</sup>) were found:

- i) an anti-correlation between the *RV* of the  $H\beta$  red peak and the relative flux of the  $H\alpha$  red peak ( $P_{RV(H\beta RP), F(H\alpha RP)} = -0.85$ );
- ii) a correlation between the *RV* of the  $H\beta$  red peak and the *EW* of the  $H\alpha$  ( $P_{RV(H\beta RP), EW(H\alpha)} = 0.63$ );
- iii) a correlation between the *RV* of the central depression of the  $H\beta$  and the *RV* of the  $H\alpha$  violet peak ( $P_{RV(H\beta CD), RV(H\alpha VP)} = 0.77$ );

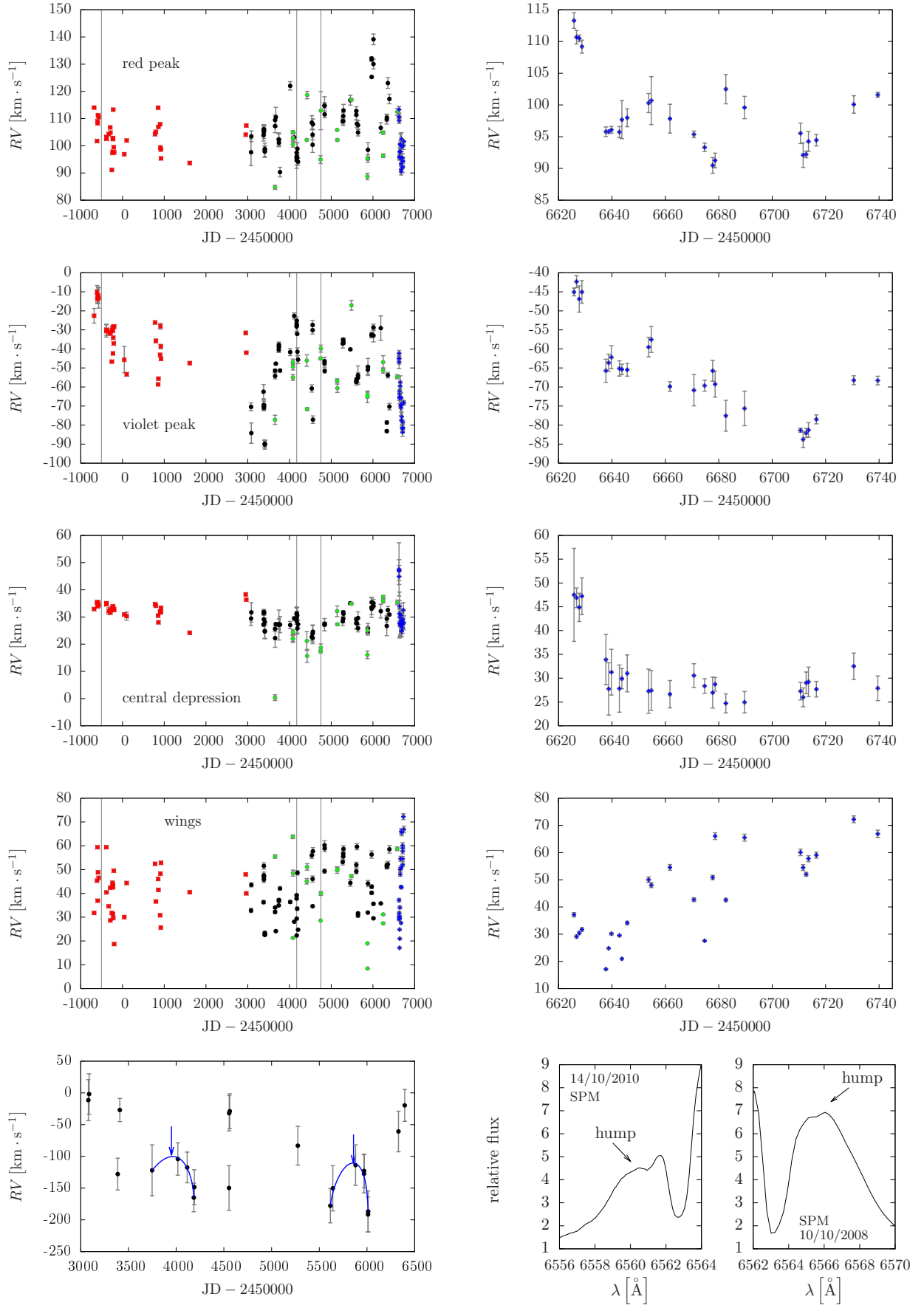


**Fig. 9.** RVs of the H $\alpha$  features. The right panels show observations obtained at TCO during the last season in detail. RVs of the red peak, the violet peak, the central depression, wing, and humps are shown from top to bottom. Parabolic fits to the RV variations of the humps detected during two seasons are shown by the solid lines with arrows. The vertical lines indicate the same epochs as in Fig. 7.



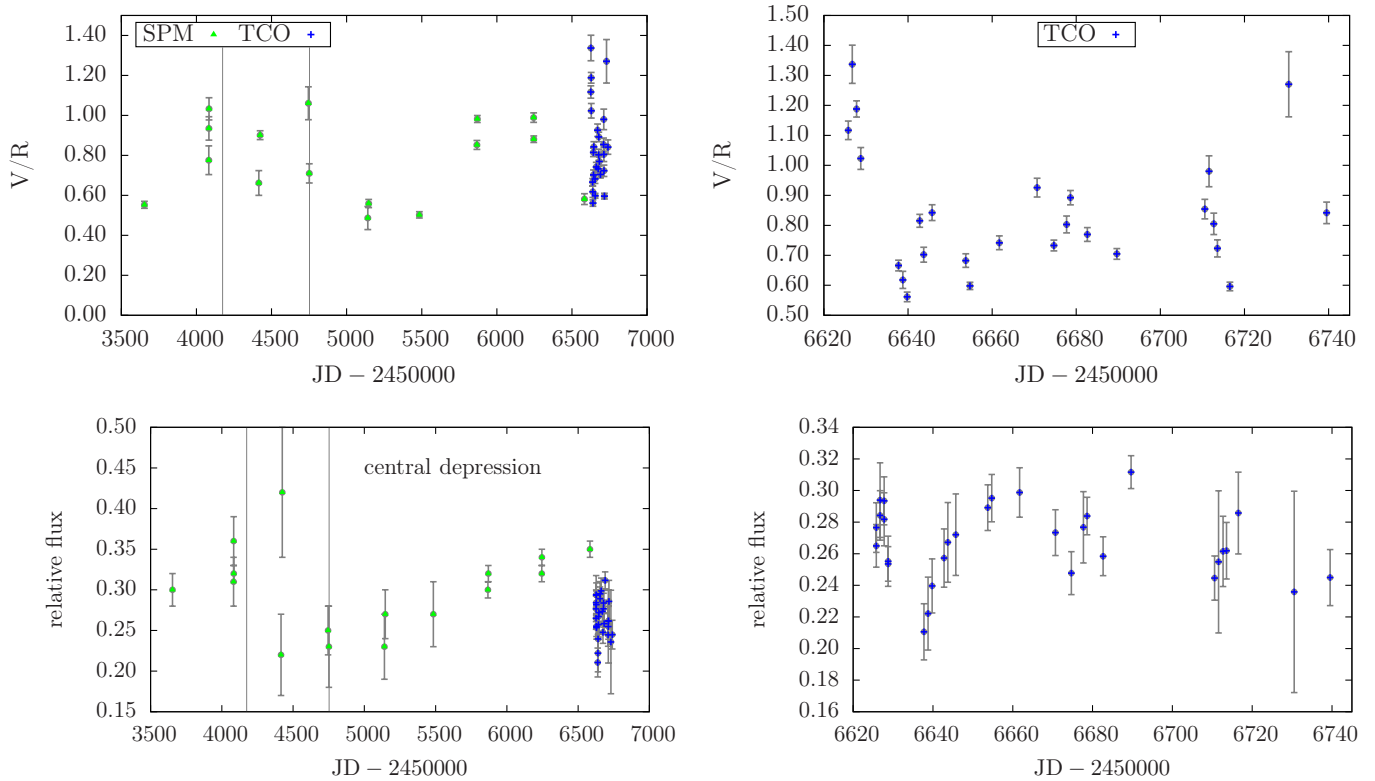


**Fig. 13.**  $V/R$  and relative flux of the central depression of the  $H\beta$  line. The vertical lines indicate the same epochs as in Fig. 7.

- iv) a correlation between the relative fluxes of the violet peak of both lines ( $P_{F(H\beta VP), F(H\alpha VP)} = 0.86$ );
- v) suggested dependencies ( $P \sim \pm 0.6$ ), which have to be proved in the future. Because they are important for the study of the system dynamics, we list them: ( $RV(H\beta RP), RV(H\alpha VP)$ ); ( $RV(H\beta CD), F(H\alpha RP)$ ); ( $RV(H\beta CD), EW(H\alpha)$ ); ( $RV(H\beta VP), RV(H\alpha RP)$ ).

#### 4.4. [O I] lines

The forbidden lines are formed in very low-density media. It is supposed to be in the outer regions, which are not significantly affected by the processes that occur close to the star. The forbidden lines are good tracers of this matter. Because the [O I]  $\lambda\lambda$  6300 and 6364 Å lines have an identical upper level, its flux ratio in the optically thin static medium is given only by the Einstein probability coefficient of the spontaneous emission and frequency of the lines,  $[F_{\text{rel}}(\text{O I}(6300)) - 1] : [F_{\text{rel}}(\text{O I}(6364)) - 1] \approx 3 : 1$ . This ratio decreases with increasing optical depth up to the limiting value of 1 (e. g. Li & McCray 1992).

The variability of the [O I]  $\lambda\lambda$  6300 and 6364 Å lines has not been described well to date. Merrill (1931) detected only the [O I] 6300 Å line in his ten-year study of HD 50138; the [O I] 6364 Å line was very faint. However, any conclusions are somewhat uncertain because photographic plates were not very sensitive in the red part of the spectra at that time. Other measurements of these lines are summarised in Tables 8<sup>e)</sup> and 9<sup>e)</sup>.

We are limited in our study of the long-term behaviour of these lines because the [O I] 6300 Å line is not present in the spectra from RO. To measure the  $EW$ , relative fluxes, and  $RV$ s we fit a Gaussian function (Sect. 3, ii, iii) to both [O I]  $\lambda\lambda$  6300 Å and 6364 Å lines. The measured values of the  $EW$  and relative

fluxes are shown in Figs. 17 ([O I] 6300 Å) and 18 ([O I] 6364 Å). These quantities can serve as tracers of the dynamics of the outer regions. The flux ratio (Fig. 19) is close to three in our spectra, which allows us to consider these lines as optically thin. Therefore, the change of the line shape due to the velocity field will change the relative flux, but the effect on the  $EW$  will be negligible. Our measurements show that both the  $EW$  and relative fluxes follow the same law.

It is not possible to say anything about the behaviour of the  $EW$  of these forbidden oxygen lines on longer timescales than is present in our data because the published measurements (Table 9<sup>e)</sup>) cover the interval of our observations.

The  $RV$ s for [O I] 6300 Å (Fig. 20) and for [O I] 6364 Å (Fig. 21<sup>e)</sup>) are almost constant except for the night of 16 January 2005. On that night a series of short exposures (600 and 900 s) was obtained. The  $S/N$  ratio was low (approximately 60) and rebinning could have played an important role.

Because the forbidden lines are formed in the outer parts of the circumstellar media, and their  $RV$ s show small variations, it is possible to take the average as a rough estimate of the  $RV$  of the system  $rv_{\text{sys}} = 40 \pm 4 \text{ km s}^{-1}$ . This value is obtained from the Ondřejov data with the exclusion of the night of 16 January 2005. The average of the  $RV$ s of both [O I] lines is almost identical,  $rv_{\text{[O I] 6300}} = 38 \pm 2 \text{ km s}^{-1}$  and  $rv_{\text{[O I] 6364}} = 41 \pm 3 \text{ km s}^{-1}$ . To see the behaviour on longer timescales, we summarise published  $RV$ s of these lines in Table 8<sup>e)</sup>. Unfortunately, only three observations are outside of our time interval. One such measurement from outside our sampling interval was from December 1972 (Andrillat & Houziaux 1972). This low-resolution (40 Å/mm) spectrum is the only one that shows a significant difference of  $RV$ s between the two [O I] lines. All observations show that the  $RV$ s of the [O I] lines change only slightly around the value, which is stable for almost 70 years.



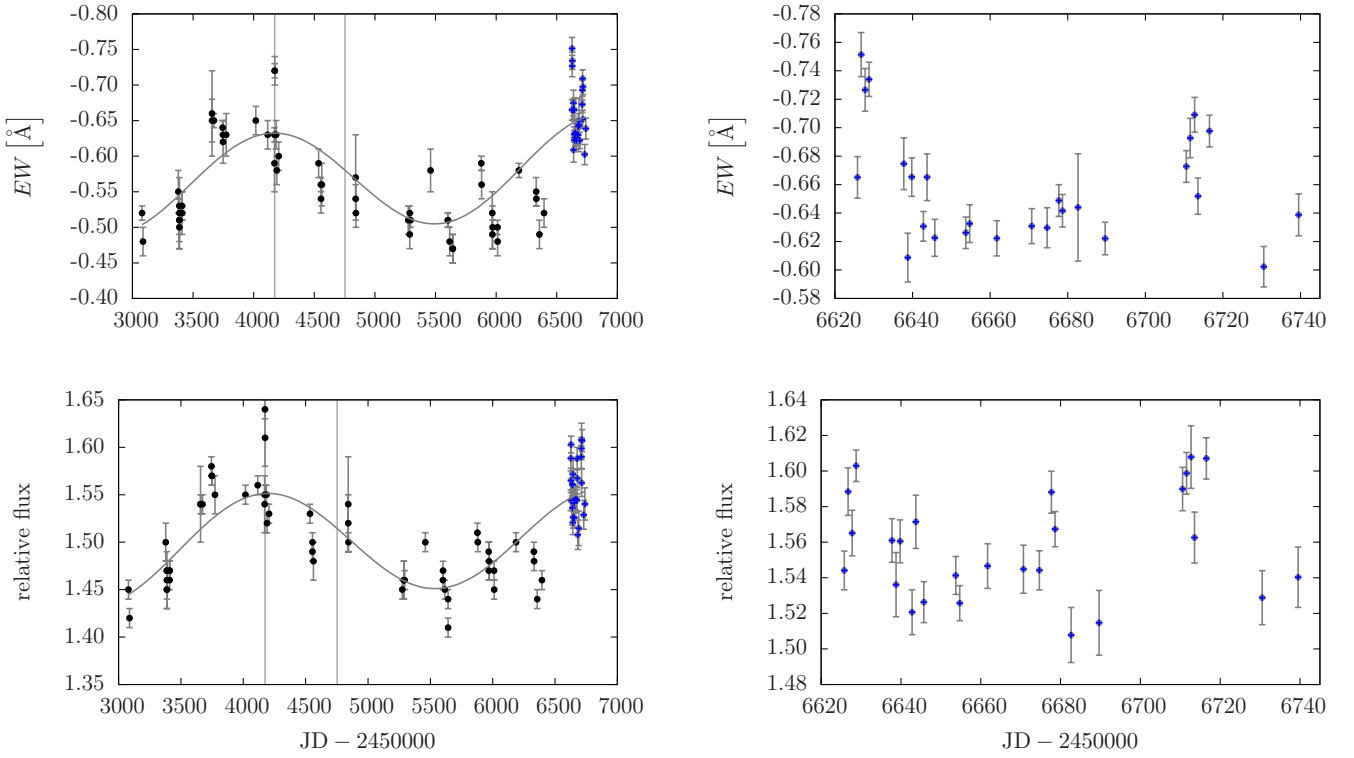


**Fig. 17.** *EW* and relative flux of the [O I] 6300 Å line. The plotted curve is a fit of two sine functions with fixed periods found by the period analysis of the H $\alpha$  *EW*.

To describe the changes of the optical depth of the forbidden oxygen lines, we plot in Fig. 19 the net flux ratio  $(F_{[\text{O I}]6364} - 1)/(F_{[\text{O I}]6300} - 1)$ . Since the flux can be affected by the velocity field we also present the ratio of the *EW*s. The figures show that the medium in the forbidden oxygen line forming region has been optically thin for more than a decade.

Even if the optical depth of the [O I] lines can be considered optically thin and *RV*s have been constant for a long time, the lines themselves are not stable (see Figs. 17 and 18) as was thought in the past. The detailed connection between the individual lines, and hence their line forming regions, is discussed in Sect. 4.8.

#### 4.4.1. Correlation between [O I] and H $\alpha$ lines

We find important connections between [O I]  $\lambda$  6300 Å and H $\alpha$  line (Fig. 22<sup>e</sup>) and Table 10<sup>e</sup>). Moreover, we identify three different time epochs determined by the *RV* of the central depression. The same time intervals also show the *V/R* ratio changes of the H $\alpha$  line. Distinct epochs are unambiguously determined when  $V/R > 1$ . Even if the number of observations in a given epoch is small, the size of the changes is significant, indicating different behaviour in different epochs similar to LBVs.

The Pearson correlation coefficients of individual epochs are summarised in Table 10<sup>e</sup>). This table contains only the *EW* and *RV* of [O I] 6300 Å because the results for the relative flux are the same thanks to their strong correlation.

Here we present the result for the Ondřejov and TCO data:

- i) a correlation of the *EW*s;
- ii) an anti-correlation between the relative flux of the H $\alpha$  red peak and the *EW*/relative flux of [O I] 6300 Å;
- iii) a weak correlation between the *RV* of the H $\alpha$  red peak and the *EW*/relative flux of [O I] 6300 Å;

- iv) an anti-correlation between the relative flux of the H $\alpha$  violet peak and the *EW*/relative flux of [O I] 6300 Å;
  - v) no correlation between the *RV* of the H $\alpha$  violet peak and the *EW*/relative flux of [O I] 6300 Å.
- We found a strong dependence in the first epoch determined by  $JD = 2454650$ , when  $V/R > 1$ ;
- vi) no correlation between the *RV* of the H $\alpha$  red peak and the *RV* of [O I] 6300 Å;
- the data show very different behaviour in different epochs.

#### 4.5. Si II $\lambda\lambda$ 6347 and 6371 Å lines

The Si II  $\lambda\lambda$  6347 and 6371 Å lines have always been observed in absorption with an occasional appearance of a red or blue emission component. The inverse P Cygni profile of these lines was reported by Borges Fernandes et al. (2009) in March and October 2007 in the FEROS spectra ( $R \sim 55\,000$ ). Borges Fernandes et al. (2012) described the rapid night-to-night variability from a nine-day campaign in February 2011 taken with the HERMES spectrograph ( $R \sim 85\,000$ ).

Most of our spectra showed an absorption line with a blue-shifted emission wing. After the correction for the *RV* ( $rv_{\text{sys}} = 40 \pm 4 \text{ km s}^{-1}$ , Sect. 4.4), we were able to distinguish a real inverse P Cygni profile, which was observed frequently. With almost the same frequency, a pure absorption line was observed. Our present observations have very rarely included either symmetric emission lines or an absorption line with a red emission wing. The behaviour of both lines is very similar, but the absorption part of the inverse P Cygni profile of the Si II 6371 Å line is usually shifted further to the red than that of the 6347 Å line. The chosen line profiles of the stronger Si II 6347 line are plot-

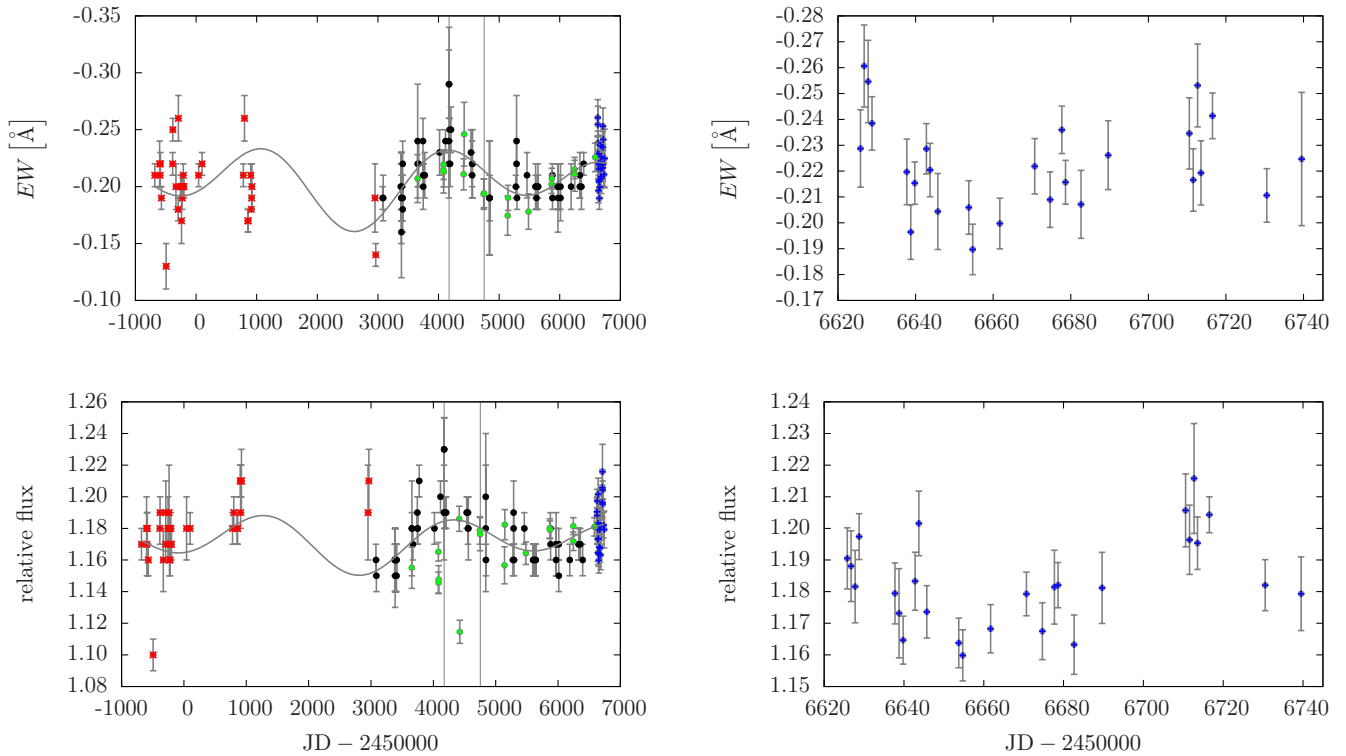


**Fig. 18.** *EW* and relative flux of the [O I] 6364 Å line. The fit of the linear combination of two sine functions is shown. However, the periods were adopted from the analysis of the *EW* of the H $\alpha$  line to prove the connection between the line-forming regions.

ted in Fig. 23 (bottom panel), and its variability is shown in its grey-scale representation (Fig. 23, upper panel).

Owing to the complicated structure of these lines, we did not measure the *RV* and *EW*. It is important to note, however, that these lines can be crucial for future modelling because they trace deep layers of the circumstellar media. For this reason we provide all of our spectra at the CDS database.

#### 4.6. He I $\lambda\lambda$ 5876 and 6678 Å lines

The He I  $\lambda\lambda$  5876 and 6678 Å lines exhibit behaviour that is similar to the Si II lines. The rapid night-to-night variability is described by Borges Fernandes et al. (2012). During the nine-day campaign of February 2011 with the HERMES spectrograph ( $R \sim 85\,000$ ), they observed variations of the absorption profile of the He I 6678 Å line. Our data (Fig. 24) show a pure absorption profile, usually red-shifted, but more frequently an inverse P Cygni profile (relative to the system radial velocity  $rv_{\text{sys}}$ , Sect. 4.4). The absorption line showed an symmetric emission wing only once.

The second line, He I 5876 Å, has been studied more frequently because of its position close to the NaD doublet. The line also shows a strong variability. An inverse P Cygni profile was reported by Bopp (1993) in spectra taken in 1992 and by Borges Fernandes et al. (2009) in the FEROS spectra from 27 October 1999. The absorption with a weak violet wing was described by Jaschek & Andrillat (1998) in spectra taken between 1989 and 1996 at Haute Provence observatory. Asymmetric absorption was noticed by Grady et al. (1996) in January 1995. A detailed study of the variability of the He I 5876 Å line was done by Pogodin (1997) on the data from 15 - 18 March 1994 taken at the CAT telescope using the CES spectrograph. During these four nights the line showed a pure absorption pro-

file, double-peaked emission, and an inverse P Cygni profile. We were able to study this line in the spectra from RO. Mostly we detected an inverse P Cygni profile (relative to the system radial velocity  $rv_{\text{sys}}$ , Sect. 4.4), and we detected a pure absorption a few times. The changes of the line-profile shape are shown by a grey-scale representation in Fig. 25.

#### 4.7. Fe II $\lambda\lambda$ 6381 and 6384 Å lines

These two lines are too faint to be measured accurately in our spectra, but a few notes on the long-term behaviour of these lines can be useful for the future study of HD 50138. We always observe both lines in emission, with a slight variability in intensity and position. The variability of the stronger Fe II 6384 Å line is shown in the grey-scale representation in Fig. 26<sup>e</sup>). When the line reached its minimum in intensity, the minimum intensity was also reached in the Si II  $\lambda\lambda$  6347, 6371 Å, He I 6678 Å lines, and the red peak of the H $\alpha$  line.

#### 4.8. Correlation between individual lines and events

To trace the important events through our observations, we plot the maxima and minima of the individual measured quantities in the time diagram (Fig. 27). Moreover, the maximum and minimum of the H $\alpha$  *EW* and maximum of the *V/R* ratio are indicated in all the relevant figures (vertical grey lines).

In Sects. 4.2.5, 4.3.2, and 4.4.1 we discussed the correlations between individual quantities in detail. Our analysis indicates that the behaviour of the system was different in different epochs. This kind of variability is seen in other spectral studies such as studies of LBVs.

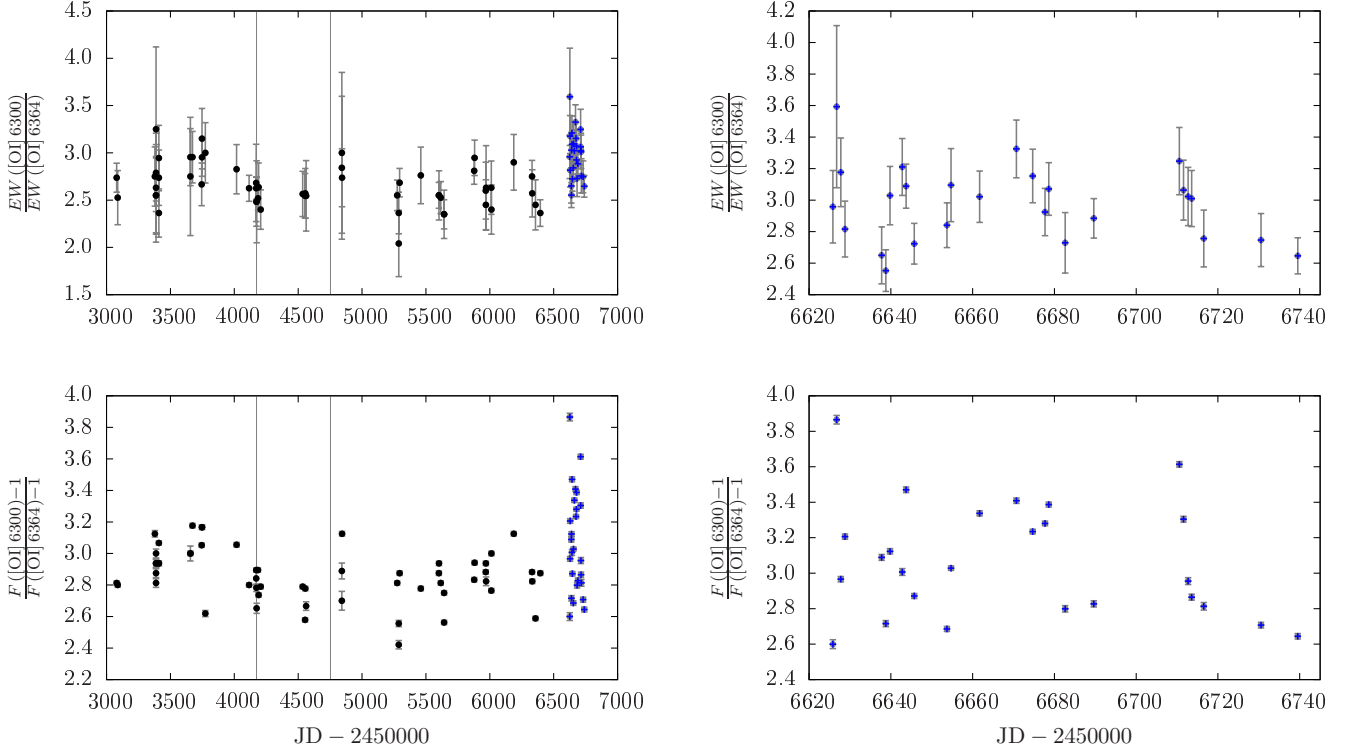


**Fig. 19.** Ratio of  $EW$  (upper panel) and net line fluxes  $F$  (lower panel) for the forbidden oxygen lines.

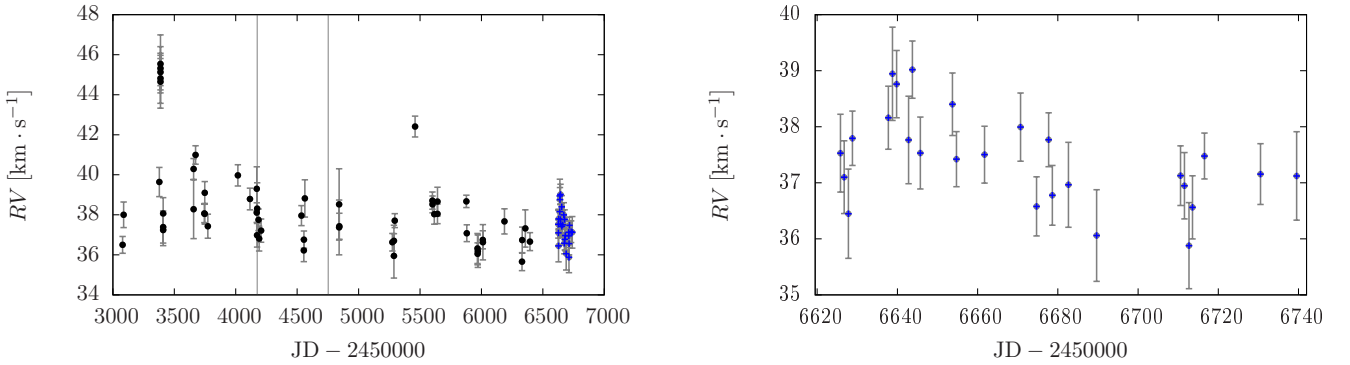


**Fig. 20.**  $RV$  of  $[O\ I]\ 6300\ \text{\AA}$ . The deviated points are the measurement from one night ( $JD\ 2\ 453\ 387$ ) with a pure  $S/N$  around sixty.

The number of measurements in the individual epochs is not sufficient (from 25 to 35) for satisfactory statistics. The measured data were separated by the  $RV$  of the central depression, which is connected with the speed of the wind. The difference between individual epochs is too high to be simply statistical error (Tables 7<sup>e</sup>) and 10<sup>e</sup>). The largest deviation was detected in the period from  $JD\ 2\ 453\ 079$  to  $2\ 454\ 650$ , which is the first half of the uniform Ondřejov data set. Moreover, the end of this period is determined by the maximum of the  $V/R$  changes in the  $H\alpha$  line ( $V/R > 1$ ). Figure 27 shows that  $H\alpha\ V/R > 1$  occurred at the same time as the minimum of the  $H\alpha$  red peak, the maximum of the  $H\beta$  peak's  $RV$ s, and the maximum of the  $V/R$  of the  $H\beta$ . Therefore, the different behaviour of the object in different epochs should be taken as one of the important criteria in the modelling of HD 50138 system.

It was impossible to describe the behaviour of the  $He\ I\ 6678\ \text{\AA}$  and  $Si\ II\ \lambda\lambda\ 6347, 6371\ \text{\AA}$  lines in a simple way because of their complicated line profiles. However, these lines

show a similar behaviour. The most important event occurred on  $JD\ 2\ 454\ 554.50$  when these three lines showed an extremely wide and deep red wing. At the same time, the  $RV$  of the central depression of the  $H\alpha$  line reached its most negative value.

#### 4.9. Long-term and short-term periodicity

The period analysis was done using the *scargle* and *HEC27* codes (Sect. 3, vi). We searched for a long-term periodicity in a time interval of a thousand days and for a short-term periodicity after data detrending (by dynamical averaging or long-term period subtraction).

The most important periods are revealed in the  $EW$  of the  $H\alpha$  line. The combination of the two most significant peaks of the power spectrum (Fig. 28<sup>e</sup>), top panel) fit the measured values well (Fig. 7; upper panel) and give the period estimates of  $3\ 200 \pm 500$  and  $5\ 000 \pm 500$  days. The same periods are found in the  $RV$  of the violet peak. The violet peak data also show an ad-

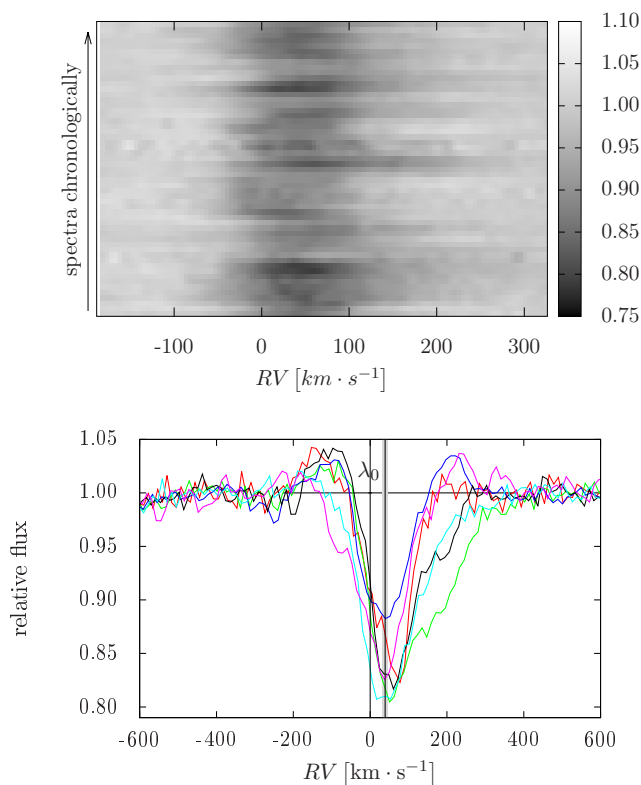


**Fig. 23.** Variations of the Si II 6347 Å line. *upper panel:* Grey-scale representation. *bottom panel:* Typical profiles (Ondřejov data, R~12500). The sharp vertical line denotes the laboratory wavelength  $\lambda_0$ . The position of  $\lambda_0$  in the frame connected with the HD 50138 system is also plotted together with its error bar. The line shift is determined by the RV of the system  $rv_{\text{sys}} = 40 \pm 4 \text{ km s}^{-1}$  based on the RVs of the [O I]  $\lambda\lambda$  6300, 6364 Å lines.

ditional period of  $1000 \pm 600$  days. The red peak and central depression variability supports this result ( $P = 3\,000 - 4\,000$  days). It is possible to identify a period of 3 200 days in the EWs of [O I] 6300 Å. Because of the reduced data set for the [O I] 6300 Å line, we use the exact values of periods found in the H $\alpha$  EW dependence to fit the [O I] 6300 Å values. The resulting fit is shown in Fig. 17 for EWs and for relative fluxes.

After subtraction of the global trend (Fig. 28, bottom panel), a period of  $300 \pm 50$  days was found in the EW of the H $\alpha$  line. Changes in the V/R of H $\alpha$  show a period of  $600 \pm 50$  days; a less significant period of approximately  $50 \pm 10$  days was found only by HEC27. This value is similar to the value of  $60 \pm 10$  days, which is shown by the RVs of the H $\alpha$  red peak and central depression. HEC27 indicates the shortest period of  $20 \pm 5$  days in the RVs of the H $\alpha$  peaks and central depression.

To search for short-term periods, we use the TCO data set because its time coverage is better. This allows us to detect a periodicity of the order of days to tens of days. We found no distinct period. The RV of the H $\alpha$  red peak suggests 20 and 35 days periods and the central depression of the H $\beta$  line 9 and 33 days, but they are not able to fit the data well.

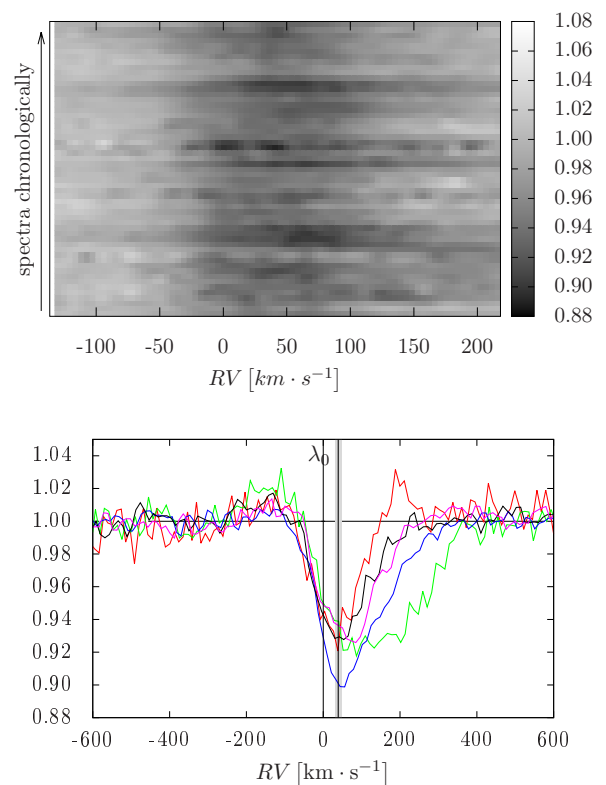


**Fig. 24.** Variations of the He I 6678 Å line. *upper panel:* Grey-scale representation. *bottom panel:* The typical line profiles are plotted from the spectra taken at the Ondřejov Observatory (R~12 500). The central wavelength is denoted in the laboratory frame  $\lambda_0$  and in the frame connected with the object. The shift is determined by the system RV  $rv_{\text{sys}} = 40 \pm 4 \text{ km s}^{-1}$  obtained from the RVs of the [O I]  $\lambda\lambda$  6300, 6364 Å lines.

## 5. Discussion

Our spectra of HD 50138 showed a strong variability of this object. A detailed discussion of the influence of the individual physical phenomena on the spectral line profiles is presented in this section, but first it is necessary to briefly describe the EW variability in the context of the photometry.

### 5.1. EW variations vs. photometry

Changes in the line EWs result not only from changes in the lines themselves, but also from the variations of the continuum radiation. This effect must be taken into account in the interpretation of the EW variability.

In this regard it is essential to consider the very important work of Halbedel (1991). She photometrically monitored HD 50138 for five years, from 1985 to 1991. During the observing campaign, the brightness of the star remained almost constant. The maximum variation in the V-band was 0.11 mag. The observations were also carried out eleven days before the discovery of a new shell phase by Andriolat & Houziaux (1991) and forty days after that. No significant photometric changes were found. The photometric variability from another observational campaign (Sect. 1) was also found only on small scales. This indicates that the observed line variability is connected mainly with the line emissivity and opacity of given transitions.



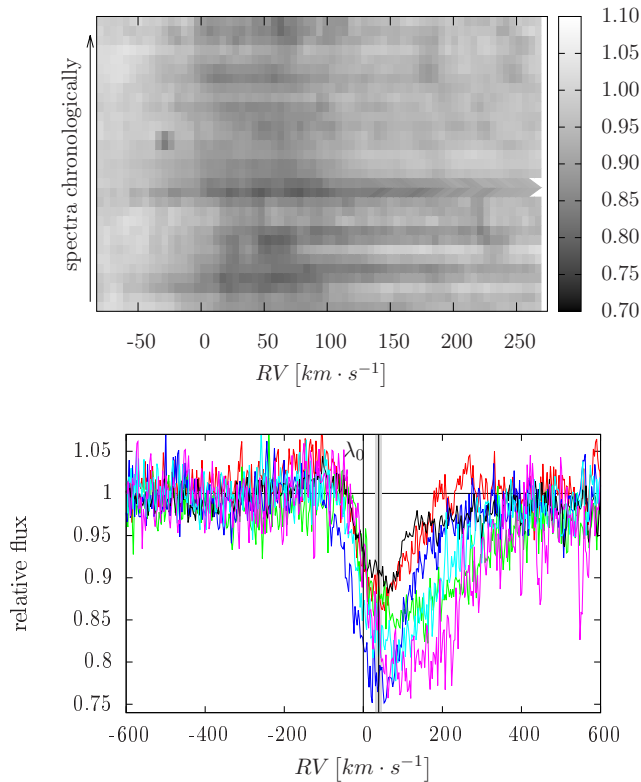


**Fig. 25.** Variations of the He I 5876 Å line. *upper panel:* Grey-scale representation. *bottom panel:* The typical line profiles were selected from the spectra taken at SPM ( $R \sim 18\,000$ ). The vertical lines denote the central wavelength at laboratory frame ( $\lambda_0$ , sharp line) and at the frame connected with HD 50138. The line shift and its error bar are determined by the RV of the system  $rv_{\text{sys}} = 40 \pm 4 \text{ km s}^{-1}$  based on the RVs of the [O I]  $\lambda\lambda$  6300, 6364 Å lines.

## 5.2. System dynamics vs. correlation of measured quantities

The relationships between individual measured line parameters contain the information about the dynamics of the circumstellar matter, which makes them very important for the construction of the model of HD 50138.

Most of the strong correlations discussed here can be qualitatively explained by changing the speed of the expansion velocity – the correlation between the RVs of the H $\alpha$  peaks and the central depression (Sect. 4.2.5 *iii*, Fig. 11<sup>e</sup>), the RV of the H $\beta$  red peak and the flux of the H $\alpha$  red peak (Sect. 4.3.2 *i*, Fig. 16<sup>e</sup>), upper left panel), the RVs of the H $\beta$  central depression and the H $\alpha$  violet peak (Sect. 4.3.2 *iii*, Fig. 16<sup>e</sup>), bottom left panel), and the flux of the H $\alpha$  red peak and the EW and relative flux of the [O I]  $\lambda$  6300 Å line (Sect. 4.4.1 *ii*, Fig. 22<sup>e</sup>), right panel, upper graph).

The effect of changing line opacities and emissivities is visible on the relative fluxes of both peaks and central depression of the H $\alpha$  line (Sect. 4.2.5 *ii*, Fig. 10<sup>e</sup>), and the EWs of the H $\alpha$  and [O I]  $\lambda$  6300 Å line (Sect. 4.4.1 *i*, Fig. 22<sup>e</sup>), left panel, upper graph).

Important for the determination of the region of the forbidden line formation can be the dependence between the RVs of the H $\alpha$  red peak and [O I] (Sect. 4.4.1 *vi*, Fig. 22<sup>e</sup>), right panel, bottom graph). The fact that they are not correlated could be explained by changing the speed of the outflow, but with the assumption that the forming region of the forbidden lines is far

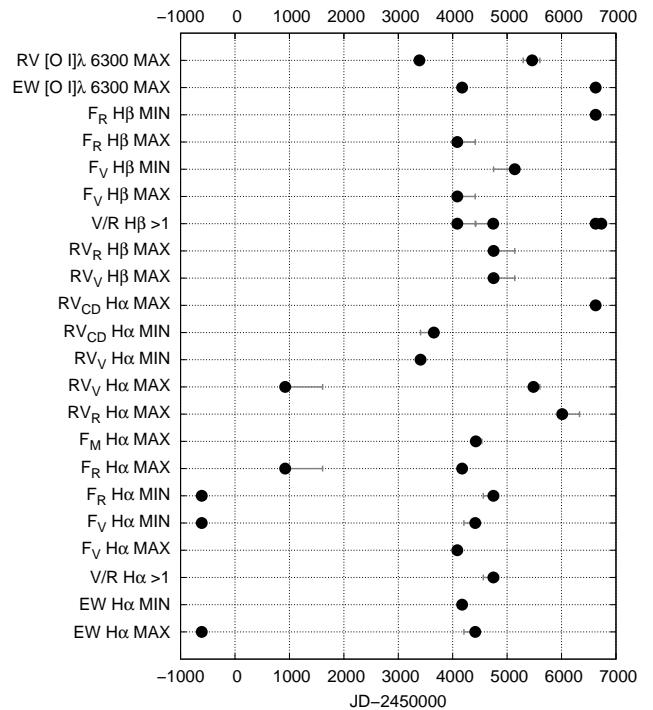


**Fig. 27.** Timeline of characteristic events in the spectra. *RV*, *EW*, and *F* denote radial velocity, EW, and flux, respectively. Subscripts *R*, *V*, and *CD* refer to the red peak, violet peak and central depression of the line profile.

from the central object, whose projection is almost negligible in this region.

Other correlations found in the present study have no straightforward interpretation since they are affected by several processes. Nevertheless, the well-established correlations confirm that the material outflow is present in the system, but it is unclear whether they are caused by a variable wind or by an expansion of the disc.

A rough guess of the system geometry is shown in Fig. 27 summarising the timeline of the maxima and minima of individual quantities. Particularly, we point out that the maxima and minima correspond to the *V/R* of the H $\beta$  line greater than one. This behaviour could not be explained by a simple binary model with a symmetric disc. A highly distorted disc with a spiral arm fits the situation better (Fig. 29<sup>e</sup>). The line-profile variations are affected by orbital and precession period (Foulkes et al. 2004; Regály et al. 2011). Similar geometry show some short periodic cataclysmic variables, SU UMa stars, or some of the transient low-mass X-ray binaries.

## 5.3. Wind

Clear evidence of outflowing material is the detection of a P Cygni profile. This line-profile shape was observed, for example in the Mg II resonance doublet in IUE spectra (1978 – 1982; Hutsemekers 1985). We did not detect a P Cygni profile in any of the lines in our optical spectra. On the other hand, there is indirect evidence supporting material outflow. The central depression of the H $\alpha$  line is always blue-shifted with respect to the system velocity defined by the forbidden oxygen lines. Signatures of the wind can also be seen in Fig. 9. On the right-hand side of the figure there is a clear correlation of the RVs of both

peaks and the central depression (Table 7<sup>e</sup>). A possible wind effect can be seen in the *RV* variations of the violet peak, which are twice as large as those of the red peak and the central depression.

However, the situation in HD 50138 is more complicated. Previous studies, as well as our observations, show signatures of material inflow and expanding layers.

#### 5.4. Expanding layers

Expanding layers with periodic changes of the expansion velocity were found by Doazan (1965). Almost two decades later Hutsemekers (1985) detected a slowly expanding decelerating layer in IUE spectra (1978 – 1982).

Our long-term observations show that the model of the system has to be even more complex. The *RV*s of the central depression and red peak of the  $H\alpha$  line (Fig. 9) show, after the global trend subtraction, changes with a period of about 60 days. This is probably the same phenomenon described by Doazan (1965) in the analysis of spectra (75 Å/mm, and 100 Å/mm) taken in 1960 – 1963 at Observatoire de Haute-Provence. She found a period of 50 days, but her observing campaign was too short to describe long-term behaviour. Our data not only reveal the presence of long-term changes, but also indicate that their origin is different. A few correlation diagrams (mostly the *RV* of the red peak vs. flux of the violet peak of the  $H\alpha$  line, and flux and *RV* of the central depression of the  $H\alpha$  line) show inhomogeneous structure. It is possible to break down these diagrams based on the individual epochs in the diagram of the *RV* of the central depression (Fig. 9). In these epochs, the correlations and anti-correlations are different. It is noteworthy that splitting the observations into four sub-intervals significantly lowers the number of measurements for the statistics in individual sub-intervals. To demonstrate the size of this effect, we present the correlation coefficients for the dependence of flux of the violet peak and *EW* of the  $H\alpha$  line (Table 7<sup>e</sup>).

#### 5.5. Material infall

Material infall has also been observed in HD 50138. The most distinctive signature of this event is the detection of inverse P Cygni profiles. We found them in the  $\text{Si II } \lambda\lambda 6347, 6371$  Å, and  $\text{He I } \lambda\lambda 5876, 6678$  Å lines in several spectra. To determine if the absorption is red- or blue-shifted with respect to the HD 50138 system, we used the *RV*s of the  $[\text{O I}] \lambda\lambda 6300, 6364$  Å lines.

The inverse P Cygni profile in various lines was detected several times. Andrillat & Houziaux (1991) reported this line-profile shape at  $\text{O I } 7773$  Å on 29 December 1990. A few months later, on 10 April 1991 Bopp (1993) detected the inverse P Cygni profile in  $\text{He I } 5876$  Å. This profile of this line was also observed by Pogodin (1997) in March 1994. Grady et al. (1996) found an inverse P Cygni profile in the  $\text{C IV}$  resonance doublet  $\lambda\lambda 1548, 1551$  Å in the ultraviolet.

#### 5.6. Rotating disc

Our data show the presence of a rotating disc. We detected moving humps in both the red and violet peaks. Detection of a hump in the violet peak is more frequent, which is probably only due to its shape. The red peak is steeper, therefore small deformations are more difficult to detect. The *RV*s of the well-defined humps in the violet peak are plotted in Fig. 9. We were able to follow some temporal dependencies indicated by the blue lines

in Fig. 9. These polynomial fits show that the inhomogeneities revolve around the central object.

Evidence in support of a rotating disc were found by comparing peak separations of the Balmer lines. Even if the line-profile shape is significantly distorted by material outflow we argue that  $H\alpha$  and  $H\beta$  lines in several spectra imply a disc-like structure. The peak separation is larger for the  $H\beta$  line. This proves that the velocity is higher for the region closer to the star as in a rotating disc.

#### 5.7. Binary hypothesis

The binary origin of HD 50138 is the most favourable scenario not only for this object, but also for other FS CMa stars. It naturally explains a large amount of the circumstellar matter that can be created due to mass-transfer between the two stars. On the other hand, direct conclusive and incontrovertible evidence of the presence of the secondary component is still missing.

- i) Analysis of the *radial velocities* is not straightforward in this case because the line-profile shape is changed by the circumstellar matter suppressing the effect of the binary motion. We present here the most extensive set of measurements of *RV*s with the best temporal coverage. However, the periodogram analysis does not show a distinctive period. Observations obtained between 1920 and 1930 also did not show any simple periodicity (Merrill 1931). The variations of *RV*s measured between 1960 and 1963 were interpreted by Doazan (1965) as changes in the expansion velocity. Unfortunately, the other studies are based on only a small amount of data and are not appropriate for the period analysis.
- ii) Evidence of the binary nature of HD 50138 was found by Baines et al. (2006) in the *spectroastrometric* observations.
- iii) The *polarimetric measurements* of Bjorkman & Schulte-Ladbeck (1994) show signatures of binarity. On the other hand, these observations can also be explained by the presence of orbiting dust.
- iv) The detection of the *central quasi-emission peak* (Fig. 3<sup>e</sup>) can support the binary hypothesis. This weak emission appears almost at the systemic velocity, which indicates that the emission can originate near the Lagrangian point L1. However, this explanation is not unique. Hanuschik (1995) showed that this emission is the radiative transfer effect through the circumstellar disc, which is optically thin in the continuum and thick in the line center. A detailed discussion is presented in Rivinius (2005).
- v) A possible explanation of why the secondary companion has not been detected is that it is much fainter than the visible B-type companion. Comparison with models of non-conservative evolution of binary systems (van Rensbergen et al. 2008) shows that the initially more massive companion may lose a significant fraction of its mass and become much fainter than the initially less massive companion while still filling its Roche lobe. Since at this time the mass reversal has occurred, the hot companion has been spun up and become more massive. Therefore, it may not be easy to detect its orbital motion.

#### 5.8. Excitation waves

Our observations show that the *RV*s of the  $[\text{O I}]$  lines are constant but their *EW*s and fluxes change. This phenomenon can be explained by the presence of excitation waves in the media. This is inconsistent with photometric observations.

### 5.9. Transit-time damping

An alternative explanation of the observed phenomena described above (Sect. 5.8) is offered by a magnetic field, particularly the transit-time damping effect (Suzuki et al. 2006). They show that propagating fast waves through the rotating stellar wind that includes a magnetic field leads to the transfer of the magnetic energy into the plasma.

The conditions necessary for this effect are found in B[e] stars, namely *i*) rotation of the circumstellar matter, which leads to the creation of spiral arms; *ii*) low density, to achieve the condition of a collisionless plasma; and *iii*) a very extended volume that generates enough radiation so that it can be detected.

As the angle between the wave propagation vector and magnetic field changes due to the rotation of the circumstellar matter, the size of this effect grows and shrinks. Differing amounts of energy are transformed from the magnetic field into the plasma. Especially important are electrons, which travel quickly through the media. The different group velocity changes the electron density in different areas. The different energy and density of electrons change the level population in the different areas of the media and leads to the changing of the line intensity. A distant observer detects changes of the line intensity, but with no changes in the *RV* and the brightness; this is exactly what is observed in the [O I] lines.

However, our observations themselves do not prove that transit-time damping plays a significant role in the circumstellar media of the B[e] stars. To show this, finer time coverage and more precise photometry are needed, as well as simultaneous observations in UV and visible because of the  $L\beta$  pumping of the O I  $3d\ ^3D^0$  energy level. Decay from this level also affects [O I]  $\lambda\lambda$  6300, 6364 Å.

### 5.10. Post-merger systems

de la Fuente et al. (2015) found two FS CMA stars in the open clusters Mercer 20 and 70. This allows them to restrict the age of these stars to the interval from 3.5 to 6.5 Myr. This excludes pre- as well as post-main sequence scenarios. They were not able to detect any signature of the secondary component in the spectra, which indicates that if the stars are binaries, the luminosity ratio must be high. Alternatively, the stars could be post-merger stellar objects. The current or former binary nature of FS CMA type stars is supported by the fact that both stars were detected in the crowded regions of the clusters.

### 5.11. HD 50138 among others FS CMA stars

The variability of FS CMA stars has not been well established, but it is possible to make some statements. HD 50138 is noteworthy among FS CMA stars because of the very small variability of its brightness. On the other hand, the spectral variability is large, as it is in MWC 342 (Kučerová et al. 2013). They detected periodicity of *RV* of the central depression (4.3 years), *EW* (769 days and 2.1 years), and *V/R* changes (4 years) which are shorter but better defined than in HD 50138.

## 6. Conclusions

We obtained and analysed the spectra of the B[e] star of the FS CMA type HD 50138 over the past twenty years. Because of the huge amount of circumstellar matter, we have no direct information about the central object. Therefore a description of the variability is crucial in the study of such objects.

The present measurements show a previously unexpected behaviour. The forbidden oxygen lines are strongly correlated with the  $H\alpha$  line. Therefore, their region of formation may be located closer to each other than previously thought. The double-peaked Balmer line profiles and especially the moving humps detected in both the  $H\alpha$  and  $H\beta$  lines proved that there is a disc-like structure of the circumstellar gas around the star.

We used different methods to search for a periodicity of the measured quantities, but we detected no explicit period. We only found modest signatures of a regular periodicity of about 34 days only during one season from TCO (from 29 November 2013 to 23 March 2014). Even if the corresponding peak in the power spectra of the *RV*s of the  $H\alpha$  red peak and  $H\beta$  central depression is not very significant and the fit of measured values shows large deviations, the variations on this timescale are probably real. A period of about 30 days can also be detected in the spectra obtained from December 1920 to February 1930 by Merrill (1931). Such a timescale is compatible with a possible orbital period of a binary system with current or previous mass transfer between the components (e.g. Miroshnichenko et al. 2015).

Long-term variations can be described by a combination of two periods of 8.8 and 13.7 years. Considering the results of previous studies of long-term variability of other FS CMA stars (Polster et al. 2012; Kučerová et al. 2013), one can conclude that quasi-periodicity on timescales of several years seems to be a typical signature of these objects.

The detrending of the  $H\alpha$  *V/R* changes allows a variability to be detected of the order of 50 days, which is consistent with the results of Doazan (1965). The presence of the period on this timescale is confirmed by the *RV*s of the red peak and central depression of the  $H\alpha$  line, which exhibit a period of 60 days after the removal of a global trend.

Our long-term study shows that the object passed through several episodes of very different spectral patterns. Confirmation of the irregular behaviour of the object has important consequences. It suppresses signatures of the periodic spectral changes caused by orbital motion and complicates the confirmation (or rejection) of the binary nature of FS CMA stars. The coincidence of the extrema of measured quantities points to an asymmetric disc around the HD 50138 system. The variations of line profiles that arise from an eccentric disc are affected by orbital motion of the gas, possible precession of the disc, as well as the changes of its structure. With regard to the real data distribution, the determination of the orbital and precession periods is very complicated. Moreover, the found periods differ for prograde and retrograde disc precession. These are the reasons why the binary nature of HD 50138 could not be excluded based on our data. On the other hand, the irregular behaviour of HD 50138 can also be explained by a new hypothesis about the nature of FS CMA stars as post-merger systems (de la Fuente et al. 2015). Other ideas about the nature of FS CMA stars do not seem to be able to explain all the observed properties by including only one or two phenomena and lead to complicated scenarios.

Based on our observations and previously published results, we summarise the features that have to be described by a physically consistent model:

- i) rotating regions;
- ii) material infall;
- iii) material outflow;
- iv) episodic mass ejection;
- v) different behaviour in different epochs;
- vi) constant brightness vs. strong line-profile variability;
- vii) no regular periodicity;
- viii) quasi-periodic behaviour.



HD 50138 is a perfect laboratory for the study of stellar/binary evolution, and of various other physical phenomena such as excitation waves, (magneto-)hydrodynamical waves, and complex non-LTE effects. This star offers the unique opportunity to support the study of such complicated objects as  $\eta$  Car because some of the observed properties are similar to the LBVs. Moreover, it is bright, and close enough to obtain good interferometry and spectra with high temporal and spectral resolution.

*Acknowledgements.* We would like to thank the referee for his comments, which helped to improve the paper. We thank Steven N. Shore for his valuable and inspiring remarks and discussions. We also would like to thank Petr Harmanec for his advice and Karen Bjorkman for providing her code Scargle. We thank the Ritter observing team for taking, reducing, and sharing their data, and Pavel Mayer, Jana Alexandra Nemravová, Andrea Budovičová, and Martin Netolický for taking some of the Ondřejov spectra.

This research was financially supported by the Czech-Mexican project CONA-CYT/14/001 of the Academy of Sciences of the Czech Republic, UNCE 204020 and P209/10/0715 of Czech Science Foundation, and PAPIIT grant IN-100614. The Astronomical Institute of the Czech Academy of Science is supported by the project RVO 67985815. We acknowledge the use of the cluster SUNQUAKE maintained by the Solar Department of Astronomical Institute of the Czech Academy of Science in Ondřejov.

## References

- Allen, D. A. 1973, *MNRAS*, 161, 145
- Alvarez, M. & Schuster, W. J. 1981, *Rev. Mexicana Astron. Astrofis.*, 6, 163
- Andrillat, Y. & Fehrenbach, C. 1982, *A&AS*, 48, 93
- Andrillat, Y. & Houziaux, L. 1972, *Ap&SS*, 18, 324
- Andrillat, Y. & Houziaux, L. 1991, *IAU Circ.*, 5164, 3
- Baines, D., Oudmaier, R. D., Porter, J. M., & Pozzo, M. 2006, *MNRAS*, 367, 737
- Bjorkman, K. S., Miroshnichenko, A. S., Bjorkman, J. E., et al. 1998, *ApJ*, 509, 904
- Bjorkman, K. S. & Schulte-Ladbeck, R. F. 1994, in *Astronomical Society of the Pacific Conference Series*, Vol. 62, *The Nature and Evolutionary Status of Herbig Ae/Be Stars*, ed. P. S. The, M. R. Perez, & E. P. J. van den Heuvel, 74
- Bopp, B. W. 1993, *Information Bulletin on Variable Stars*, 3834, 1
- Borges Fernandes, M. 2010, in *Revista Mexicana de Astronomia y Astrofisica*, vol. 27, Vol. 38, *Revista Mexicana de Astronomia y Astrofisica Conference Series*, 98–99
- Borges Fernandes, M., Kraus, M., Chesneau, O., et al. 2009, *A&A*, 508, 309
- Borges Fernandes, M., Kraus, M., Nickeler, D. H., et al. 2012, *A&A*, 548, A13
- Borges Fernandes, M., Meilland, A., Bendjoya, P., et al. 2011, *A&A*, 528, A20
- Briot, D. 1981, *A&A*, 103, 5
- Carciofi, A. C. & Bjorkman, J. E. 2006, *ApJ*, 639, 1081
- Carciofi, A. C. & Bjorkman, J. E. 2008, *ApJ*, 684, 1374
- Corporon, P. & Lagrange, A.-M. 1999, *A&AS*, 136, 429
- Curé, M. 2004, *ApJ*, 614, 929
- Dachs, J., Hummel, W., & Hanuschik, R. W. 1992, *A&AS*, 95, 437
- de la Fuente, D., Najarro, F., Trombley, C., Davies, B., & Figer, D. F. 2015, *A&A*, 575, A10
- de Winter, D., van den Ancker, M. E., Maira, A., et al. 2001, *A&A*, 380, 609
- Doazan, V. 1965, *Annales d'Astrophysique*, 28, 1
- Ellerbroek, L. E., Benisty, M., Kraus, S., et al. 2015, *A&A*, 573, A77
- Foulkes, S. B., Haswell, C. A., Murray, J. R., & Rolfe, D. J. 2004, *MNRAS*, 349, 1179
- Grady, C. A., Perez, M. R., Talavera, A., et al. 1996, *A&AS*, 120, 157
- Halbedel, E. M. 1991, *Information Bulletin on Variable Stars*, 3585, 1
- Hanuschik, R. W. 1995, *A&A*, 295, 423
- Harrington, D. M. & Kuhn, J. R. 2007, *ApJ*, 667, L89
- Houziaux, L. 1960, *Journal des Observateurs*, 43, 217
- Houziaux, L. & Andrillat, Y. 1976, in *IAU Symposium*, Vol. 70, *Be and Shell Stars*, ed. A. Slettebak, 87
- Humason, M. L. & Merrill, P. W. 1921, *PASP*, 33, 112
- Hutsemekers, D. 1985, *A&AS*, 60, 373
- IAUS 70, Conti, P. S. 1976, in *IAU Symposium*, Vol. 70, *Be and Shell Stars*, ed. A. Slettebak, 447
- Jaschek, C. & Andrillat, Y. 1998, *A&AS*, 128, 475
- Kilkenny, D., Whittet, D. C. B., Davies, J. K., et al. 1985, *South African Astronomical Observatory Circular*, 9, 55
- Korčáková, D. & Kubát, J. 2005, *A&A*, 440, 715
- Kuan, P. & Kuhl, L. V. 1975, *ApJ*, 199, 148
- Kučerová, B., Korčáková, D., Polster, J., et al. 2013, *A&A*, 554, A143
- Lamers, H. J. G. L. M., Zickgraf, F.-J., de Winter, D., Houziaux, L., & Zorec, J. 1998, *A&A*, 340, 117
- Li, H. & McCray, R. 1992, *ApJ*, 387, 309
- Marston, A. P. & McCollum, B. 2008, *A&A*, 477, 193
- Mel'nikov, S. Y. 1997, *Astronomy Letters*, 23, 799
- Merrill, P. W. 1931, *ApJ*, 73, 348
- Merrill, P. W. 1952, *ApJ*, 116, 501
- Merrill, P. W., Humason, M. L., & Burwell, C. G. 1925, *ApJ*, 61, 389
- Miczaika, G. R. 1950, *Astronomische Nachrichten*, 279, 19
- Miroshnichenko, A. & Zharikov, S. 2015, <http://arxiv.org/abs/1508.06298>; submitted in *EAS Publication Series; Physics Of Evolved Star*, June 8–12 2015, Nice, France [[arXiv:1508.06298](https://arxiv.org/abs/1508.06298)]
- Miroshnichenko, A. S. 2007, *ApJ*, 667, 497
- Miroshnichenko, A. S., Zharikov, S. V., Danford, S., et al. 2015, *ApJ*, 809, 129
- Miroshnichenko, A. S., Zharikov, S. V., Manset, N., Rossi, C., & Polcaro, V. F. 2013, *Central European Astrophysical Bulletin*, 37, 57
- Monnier, J. D., Tuthill, P. G., Ireland, M., et al. 2009, *ApJ*, 700, 491
- Oudmaier, R. D. & Drew, J. E. 1999, *MNRAS*, 305, 166
- Pogodin, M. A. 1997, *A&A*, 317, 185
- Polster, J., Korčáková, D., Votruba, V., et al. 2012, *A&A*, 542, A57
- Press, W. H. & Teukolsky, S. A. 1988, *Computers in Physics*, 2, 77
- Pych, W. 2004, *PASP*, 116, 148
- Regály, Z., Sándor, Z., Dullemond, C. P., & Kiss, L. L. 2011, *A&A*, 528, A93
- Rivinius, T. 2005, *Habilitationsschrift*, Ruprecht-Karls-Universität, Heidelberg
- Savage, B. D., Wesselius, P. R., Swings, J. P., & The, P. S. 1978, *ApJ*, 224, 149
- Steffen, M. 1990, *A&A*, 239, 443
- Stellingwerf, R. F. 1978, *ApJ*, 224, 953
- Suzuki, T. K., Yan, H., Lazarian, A., & Cassinelli, J. P. 2006, *ApJ*, 640, 1005
- Swings, J. P. & Allen, D. A. 1971, *ApJ*, 167, L41
- van Rensbergen, W., De Greve, J. P., De Loore, C., & Mennekens, N. 2008, *A&A*, 487, 1129
- Vink, J. S., Drew, J. E., Harries, T. J., & Oudmaier, R. D. 2002, *MNRAS*, 337, 356
- Vollmann, K. & Eversberg, T. 2006, *AN*, 327, 862
- Votruba, V., Feldmeier, A., Kubát, J., & Rätz, D. 2007, *A&A*, 474, 549
- Yudin, R. V. & Evans, A. 1998, *A&AS*, 131, 401
- Zsargó, J., Hillier, D. J., & Georgiev, L. N. 2008, *A&A*, 478, 543



Table 2. Observing log

Ritter Observatory						
date	JD-2450000	filename	instrument	exp. [s]	S/N	observer
1993-Nov-28	-680.2251	931128Ha([OI]6300).dat	échelle	3600	70	-
1994-Feb-06	-610.3187	940206Ha([OI]6300).dat	échelle	3600	50	-
1994-Feb-16	-600.3148	940216Ha([OI]6300).dat	échelle	3600	50	-
1994-Feb-22	-594.3742	940222Ha([OI]6300).dat	échelle	3600	50	-
1994-Mar-02	-586.4597	940302Ha([OI]6300).dat	échelle	3600	50	-
1994-Mar-17	-571.4031	940317Ha([OI]6300).dat	échelle	3600	60	-
1994-Sep-18	-386.1090	940918Ha([OI]6300).dat	échelle	3600	70	-
1994-Sep-21	-383.0964	940921Ha([OI]6300).dat	échelle	3600	60	-
1994-Nov-12	-331.0622	941112Ha([OI]6300).dat	échelle	3600	50	-
1994-Dec-19	-294.2986	941219Ha([OI]6300).dat	échelle	3600	50	-
1994-Dec-22	-291.2952	941222Ha([OI]6300).dat	échelle	3600	40	-
1995-Jan-27	-255.3515	950127Ha([OI]6300).dat	échelle	3600	50	-
1995-Feb-12	-239.3537	950212Ha([OI]6300).dat	échelle	3600	50	-
1995-Feb-19	-232.3874	950219Ha([OI]6300).dat	échelle	3600	70	-
1995-Feb-22	-229.4138	950222Ha([OI]6300).dat	échelle	3600	100	-
1995-Feb-24	-227.3818	950225Ha([OI]6300).dat	échelle	3600	100	-
1995-Mar-02	-221.3767	950303Ha([OI]6300).dat	échelle	3600	90	-
1995-Mar-14	-209.4575	950315Ha([OI]6300).dat	échelle	3600	80	-
1995-Mar-24	-199.4105	950325Ha([OI]6300).dat	échelle	3600	80	-
1995-Nov-20	41.8367	951120Ha([OI]6300).dat	échelle	3600	50	-
1996-Jan-17	99.7329	960122Ha([OI]6300).dat	échelle	3600	80	-
1997-Nov-27	779.8832	971127Ha([OI]6300).dat	échelle	3600	90	-
1997-Dec-16	798.7946	971216Ha([OI]6300).dat	échelle	3600	40	-
1998-Feb-09	853.6453	980209Ha([OI]6300).dat	échelle	3600	70	-
1998-Feb-15	859.6289	980215Ha([OI]6300).dat	échelle	3600	70	-
1998-Mar-30	902.5522	980330Ha([OI]6300).dat	échelle	3600	70	-
1998-Apr-06	909.5389	980406Ha([OI]6300).dat	échelle	3600	100	-
1998-Apr-13	916.5531	980413Ha([OI]6300).dat	échelle	3600	60	-
1998-Apr-18	921.5817	980418Ha([OI]6300).dat	échelle	3600	50	-
2000-Mar-06	1609.5771	20000306Ha([OI]6300).dat	échelle	3600	50	-
2003-Nov-09	2952.8989	20031109Ha([OI]6300).dat	échelle	3600	40	-
2003-Nov-21	2964.8337	20031121Ha([OI]6300).dat	échelle	3600	40	-
Ondřejov Observatory						
date	JD-2450000	filename	instrument	exp. [s]	S/N	observer
2004-Mar-14	3079.3004	nc140022.dat	slit; 700 mm focus	1800	220	Budovičová
2004-Mar-22	3087.3256	nc220014.dat	slit; 700 mm focus	1800	140	DK
2005-Jan-07	3378.4495	oa070014.dat	slit; 700 mm focus	600	110	DK
2005-Jan-16	3387.3653	oa160020.dat	slit; 700 mm focus	900	70	VV
2005-Jan-16	3387.3784	oa160021.dat	slit; 700 mm focus	900	70	VV
2005-Jan-16	3387.3893	oa160022.dat	slit; 700 mm focus	900	70	VV
2005-Jan-16	3387.4104	oa160024.dat	slit; 700 mm focus	600	70	VV
2005-Feb-07	3409.3459	ob070006.dat	slit; 700 mm focus	900	120	MS
2005-Feb-07	3409.3568	ob070007.dat	slit; 700 mm focus	900	110	MS
2005-Feb-07	3409.3685	ob070008.dat	slit; 700 mm focus	900	110	MS
2005-Oct-13	3656.6557	oj120037.dat	slit; 700 mm focus	300	60	PS
2005-Oct-13	3656.6699	oj120038.dat	slit; 700 mm focus	1800	130	PS
2005-Oct-29	3672.6472	oj280051.dat	slit; 700 mm focus	1800	130	DK
2006-Jan-08	3744.3683	pa080035.dat	slit; 700 mm focus	3600	140	DK
2006-Jan-12	3747.5148	pa110043.dat	slit; 700 mm focus	1200	120	DK
2006-Jan-12	3747.5343	pa110045.dat	slit; 700 mm focus	1800	120	DK
2006-Feb-06	3773.3324	pb060015.dat	slit; 700 mm focus	4500	110	DK
2006-Oct-09	4017.6271	pj080065.dat	slit; 700 mm focus	2222	150	Netolický
2007-Jan-14	4115.4835	qa140071.dat	slit; 700 mm focus	2345	150	Netolický
2007-Mar-11	4171.3618	qc110030.dat	slit; 700 mm focus	1200	150	DK
2007-Mar-11	4171.3786	qc110034.dat	slit; 700 mm focus	300	60	DK
2007-Mar-13	4173.3806	qc130037.dat	slit; 700 mm focus	500	100	DK
2007-Mar-14	4174.3520	qc140004.dat	slit; 700 mm focus	600	60	VV
2007-Mar-25	4185.3377	qc250026.dat	slit; 700 mm focus	2100	140	DK

2007-Mar-30	4190.3325	qc300022.dat	slit; 700 mm focus	1800	140	Polster
2007-Apr-15	4206.2997	qd150013.dat	slit; 700 mm focus	1200	140	DK
2008-Mar-09	4535.3358	rc090021.dat	slit; 700 mm focus	1800	160	Ceniga
2008-Mar-28	4554.3230	rc280013.dat	slit; 700 mm focus	2600	140	Polster
2008-Mar-29	4555.3173	rc290019.dat	slit; 700 mm focus	1400	160	Polster
2008-Apr-05	4562.2935	rd050012.dat	slit; 700 mm focus	3000	90	Polster
2009-Jan-09	4841.4609	sa090017.dat	slit; 700 mm focus	2000	50	Polster
2009-Jan-09	4841.4869	sa090018.dat	slit; 700 mm focus	2250	50	Polster
2009-Jan-11	4843.4355	sa110048.dat	slit; 700 mm focus	2400	140	Polster
2010-Mar-19	5275.3812	tc190022.dat	slit; 700 mm focus	900	200	PS
2010-Mar-31	5287.3706	tc310009.dat	slit; 700 mm focus	900	100	PS
2010-Mar-31	5287.3868	tc310010.dat	slit; 700 mm focus	1635	80	PS
2010-Apr-07	5294.2868	td070009.dat	slit; 700 mm focus	1200	270	PS
2010-Sep-20	5459.6449	ti190046.dat	slit; 700 mm focus	1500	150	DK
2011-Feb-08	5601.4416	ub080062.dat	slit; 700 mm focus	1726	240	MS
2011-Feb-09	5602.3830	ub090044.dat	slit; 700 mm focus	1200	190	DK
2011-Feb-23	5616.3552	ub230037.dat	slit; 700 mm focus	1800	150	DK
2011-Mar-21	5642.3310	uc210020.dat	slit; 700 mm focus	900	160	DK
2011-Mar-21	5642.3472	uc210022.dat	slit; 700 mm focus	1200	160	DK
2011-Nov-12	5877.5425	uk110042.dat	slit; 700 mm focus	2700	220	DK
2011-Nov-15	5880.5281	uk140029.dat	slit; 700 mm focus	1800	160	PS
2012-Feb-10	5968.4133	vb100041.dat	slit; 700 mm focus	3600	110	DK
2012-Feb-11	5969.3987	vb110037.dat	slit; 700 mm focus	1835	130	DK
2012-Feb-12	5970.4331	vb120022.dat	slit; 700 mm focus	3600	90	DK
2012-Mar-24	6011.3095	vc240017.dat	slit; 700 mm focus	1500	160	DK
2012-Mar-25	6012.3051	vc250026.dat	slit; 700 mm focus	1200	130	DK
2012-Sep-17	6187.6396	vi160055.dat	slit; 700 mm focus	1200	160	DK
2013-Feb-06	6330.4010	wb060036.dat	slit; 700 mm focus	2261	190	PM
2013-Feb-08	6332.4040	wb080039.dat	slit; 700 mm focus	1538	120	DK
2013-Mar-05	6357.3923	wc050028.dat	slit; 700 mm focus	800	130	Zasche
2013-Apr-12	6395.2883	wd120013.dat	slit; 700 mm focus	900	200	RK & TJ
2013-Apr-12	6395.2883	wd120013.dat	slit; 700 mm focus	900	200	RK & TJ

## Observatorio Astronomico Nacional San Pedro Martir

date	JD-2450000	filename	instrument	exp. [s]	S/N	observer
2005-Oct-10	3653.9990	20051010Ha(Hb).dat	èchelle	300	70	AM & SZ
2006-Dec-12	4082.0270	20061212Ha(Hb).dat	èchelle	1980	200	AM & SZ
2006-Dec-13	4082.9700	20061213Ha(Hb).dat	èchelle	900	160	AM & SZ
2006-Dec-14	4084.0040	20061214Ha(Hb).dat	èchelle	900	180	AM & SZ
2007-Nov-10	4414.8920	20071110Ha(Hb).dat	èchelle	2220	130	SZ
2007-Nov-19	4423.9820	20071119Ha(Hb).dat	èchelle	1900	170	SZ
2008-Oct-05	4745.0190	20081004Ha(Hb).dat	èchelle	600	120	AM & SZ
2008-Oct-11	4750.9670	20081010Ha(Hb).dat	èchelle	840	180	AM
2009-Nov-05	5140.9370	20091104Ha(Hb).dat	Otro	600	110	AM & SZ
2009-Nov-11	5146.9590	20091110Ha(Hb).dat	Otro	900	130	AM & SZ
2010-Oct-14	5484.0000	20101014Ha(Hb).dat	èchelle	1200	100	SZ
2011-Nov-01	5867.0130	20111031Ha(Hb).dat	èchelle	1800	180	JLOA & ING
2011-Nov-04	5870.0030	20111103Ha(Hb).dat	èchelle	2700	180	SZ
2012-Nov-13	6244.9930	20121112Ha(Hb).dat	èchelle	5400	210	AM & SZ
2012-Nov-14	6245.9530	20121113Ha(Hb).dat	èchelle	2400	200	AM & SZ
2013-Oct-17	6583.0210	20131016Ha(Hb).dat	èchelle	600	150	SZ

## Three College Observatory

date	JD-2450000	filename	instrument	exp. [s]	S/N	observer
2013-Nov-29	6625.8120	20131128Ha(Hb.[OI]6300.6364).dat	èchelle	1200	80	AM
2013-Nov-30	6626.7420	20131129Ha(Hb.[OI]6300.6364).dat	èchelle	1440	100	AM
2013-Dec-01	6627.7780	20131130Ha(Hb.[OI]6300.6364).dat	èchelle	900	80	AM
2013-Dec-02	6628.7800	20131201Ha(Hb.[OI]6300.6364).dat	èchelle	720	100	AM
2013-Dec-11	6637.7500	20131210Ha(Hb.[OI]6300.6364).dat	èchelle	780	80	AM
2013-Dec-12	6638.7680	20131211Ha(Hb.[OI]6300.6364).dat	èchelle	450	80	SD
2013-Dec-13	6639.7920	20131212Ha(Hb.[OI]6300.6364).dat	èchelle	780	90	AM
2013-Dec-16	6642.7780	20131215Ha(Hb.[OI]6300.6364).dat	èchelle	1200	80	AM & SD
2013-Dec-17	6643.7320	20131216Ha(Hb.[OI]6300.6364).dat	èchelle	720	90	SD

2013-Dec-19	6645.7220	20131218Ha(Hb.[OI]6300.6364).dat	échelle	660	100	SD
2013-Dec-27	6653.7270	20131226Ha(Hb.[OI]6300.6364).dat	échelle	1050	90	AM
2013-Dec-28	6654.7280	20131227Ha(Hb.[OI]6300.6364).dat	échelle	1200	120	AM
2014-Jan-04	6661.7110	20140103Ha(Hb.[OI]6300.6364).dat	échelle	1260	100	AM
2014-Jan-13	6670.7080	20140112Ha(Hb.[OI]6300.6364).dat	échelle	1560	100	AM
2014-Jan-17	6674.6870	20140116Ha(Hb.[OI]6300.6364).dat	échelle	1440	90	AM & SD
2014-Jan-20	6677.7040	20140119Ha(Hb.[OI]6300.6364).dat	échelle	1260	100	SD
2014-Jan-21	6678.6400	20140120Ha(Hb.[OI]6300.6364).dat	échelle	1260	110	AM
2014-Jan-25	6682.6460	20140124Ha(Hb.[OI]6300.6364).dat	échelle	1260	80	AM
2014-Feb-01	6689.6530	20140131Ha(Hb.[OI]6300.6364).dat	échelle	1500	80	AM
2014-Feb-22	6710.5710	20140221Ha(Hb.[OI]6300.6364).dat	échelle	1680	90	AM
2014-Feb-23	6711.5730	20140222Ha(Hb.[OI]6300.6364).dat	échelle	1500	70	AM
2014-Feb-24	6712.6980	20140223Ha(Hb.[OI]6300.6364).dat	échelle	1500	60	SD
2014-Feb-25	6713.5650	20140224Ha(Hb.[OI]6300.6364).dat	échelle	1500	90	AM
2014-Feb-28	6716.5500	20140227Ha(Hb.[OI]6300.6364).dat	échelle	1800	100	AM
2014-Mar-14	6730.5280	20140313Ha(Hb.[OI]6300.6364).dat	échelle	1800	120	AM
2014-Mar-23	6739.5310	20140322Ha(Hb.[OI]6300.6364).dat	échelle	1500	80	AM

**Notes.** “AM” Anatoly Miroshnichenko, “SZ” Sergey Zharikov, “SD” Steve Danford, “DK” Daniela Korčáková, “MS” Miroslav Šlechta, “PS” Petr Škoda, “VV” Viktor Votruba, “RK” Radek Kříček, “TJ” Tereza Jeřábková

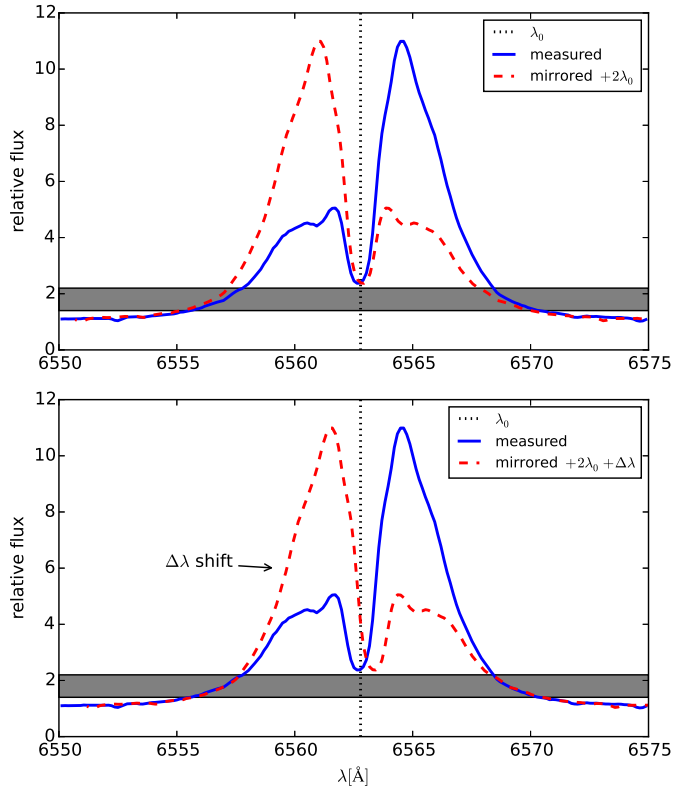


**Fig. 1.** Demonstration of the *RV* measurements using the line-profile mirroring. The best agreement of the original (blue solid line) and flipped spectra (red dashed line) is obtained by the least squares method. The grey belt defines the interval of the relative flux where the *RV* are measured. The plotted spectrum is from 14 October 2010 (SPM).



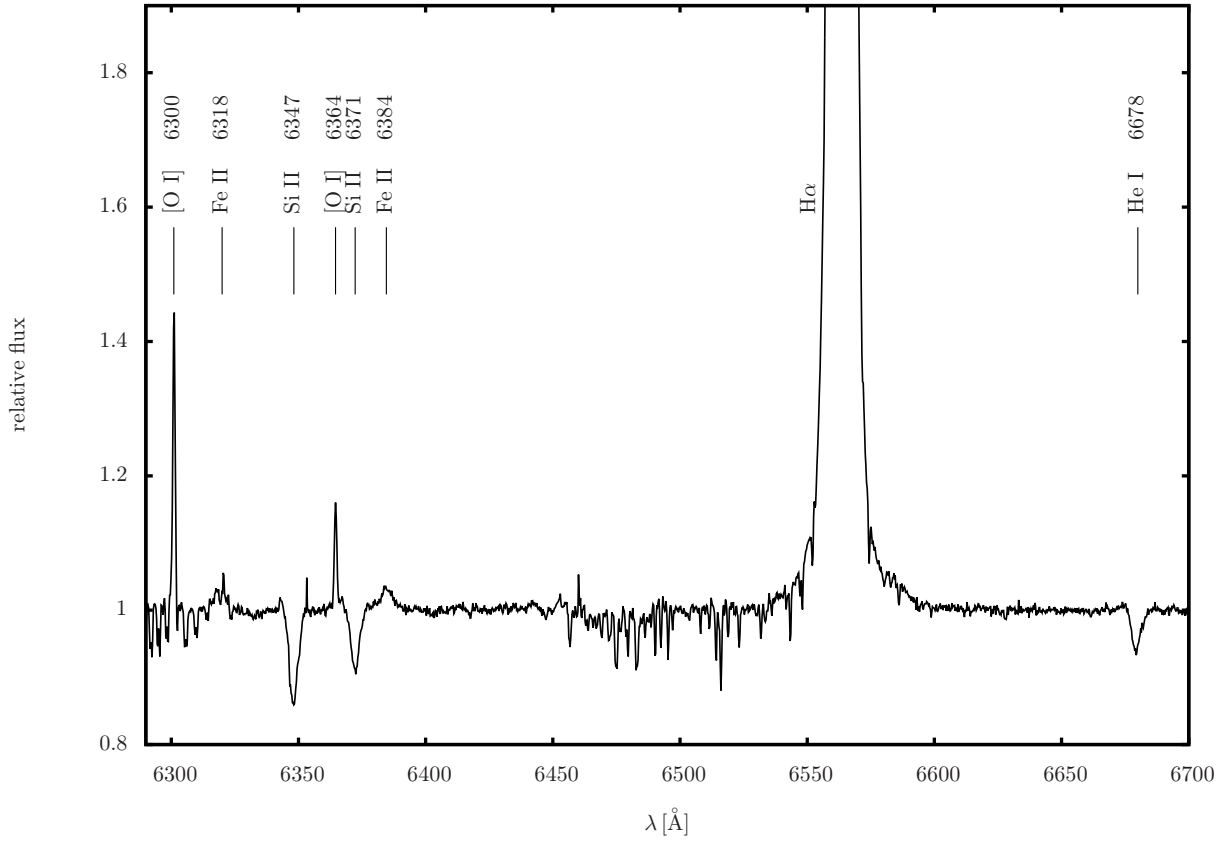


**Fig. 2.** Identification of the spectral lines based on the work of Doazan (1965) and the NIST database. The spectral interval shows the important lines chosen for the long-term study at the Ondřejov slit spectra ( $R \sim 12\,500 \text{ \AA}$ ).

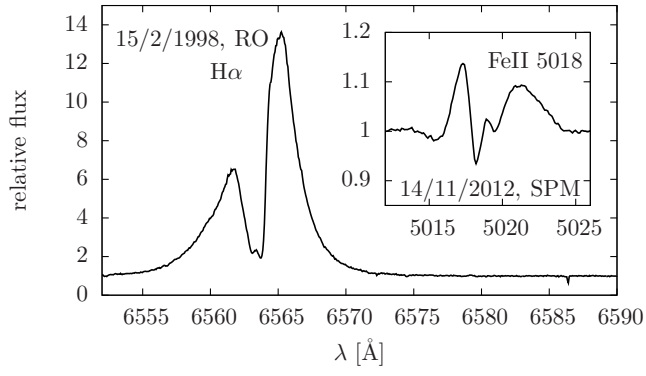


**Fig. 3.** Central quasiemission peak (CQEP) of the  $H\alpha$  (15 February 1998, RO), and Fe II 5018 Å line (14 November 2012, SPM). The CQEP were not detected simultaneously in the Fe II lines and  $H\alpha$ .

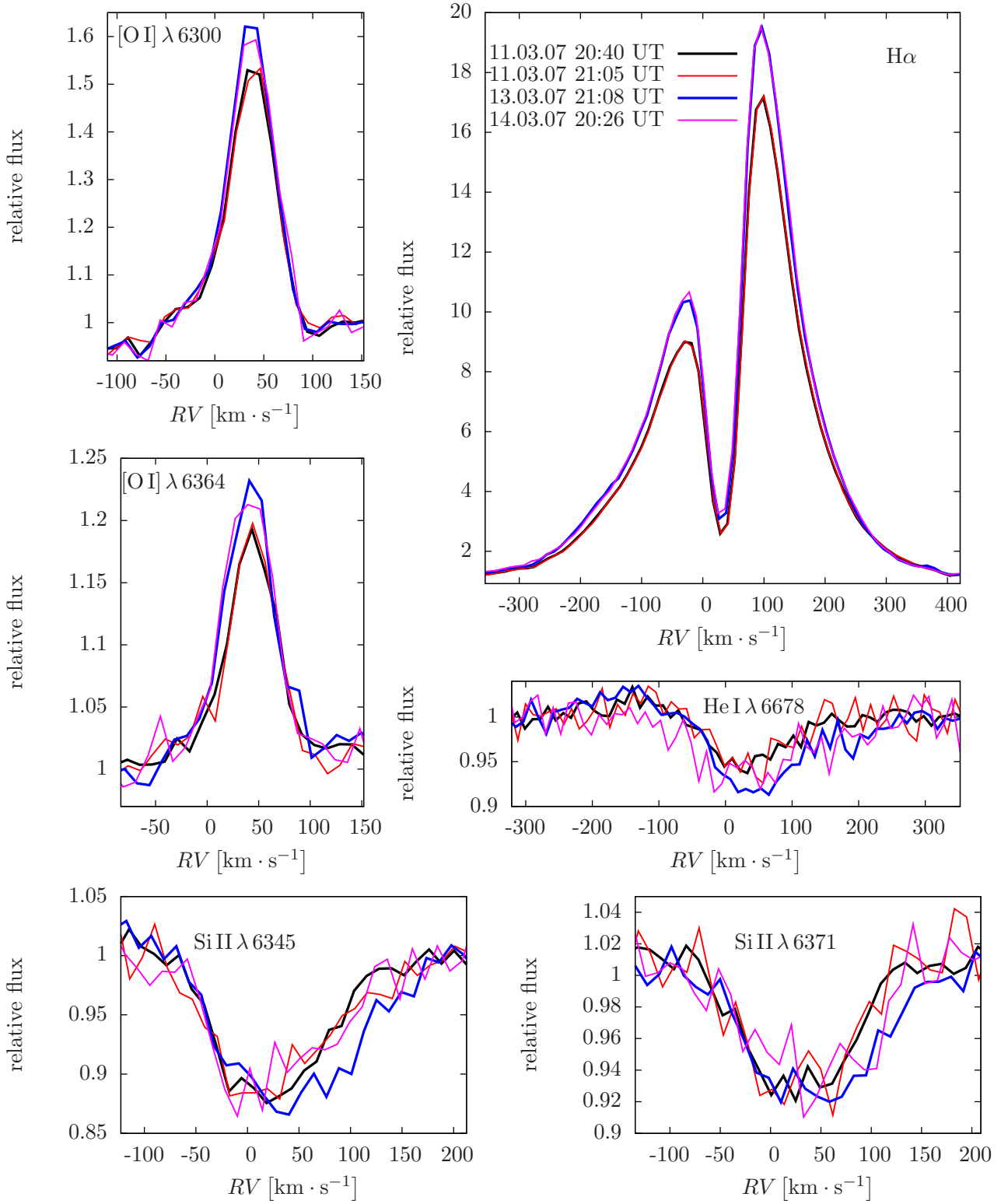


**Fig. 4.** Night-to-night spectral line changes.

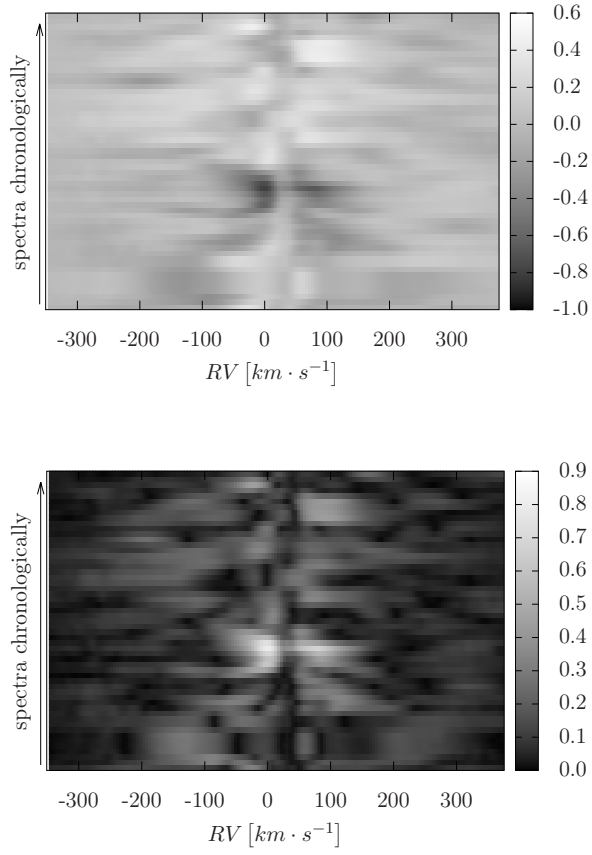


**Fig. 6.** Grey-scale representation of the H $\alpha$  line on the spectra from OO. The residuals between the given line profile and averaged line profile (upper panel). To emphasise the structures, the absolute value of the differences is plotted on the lower panel.



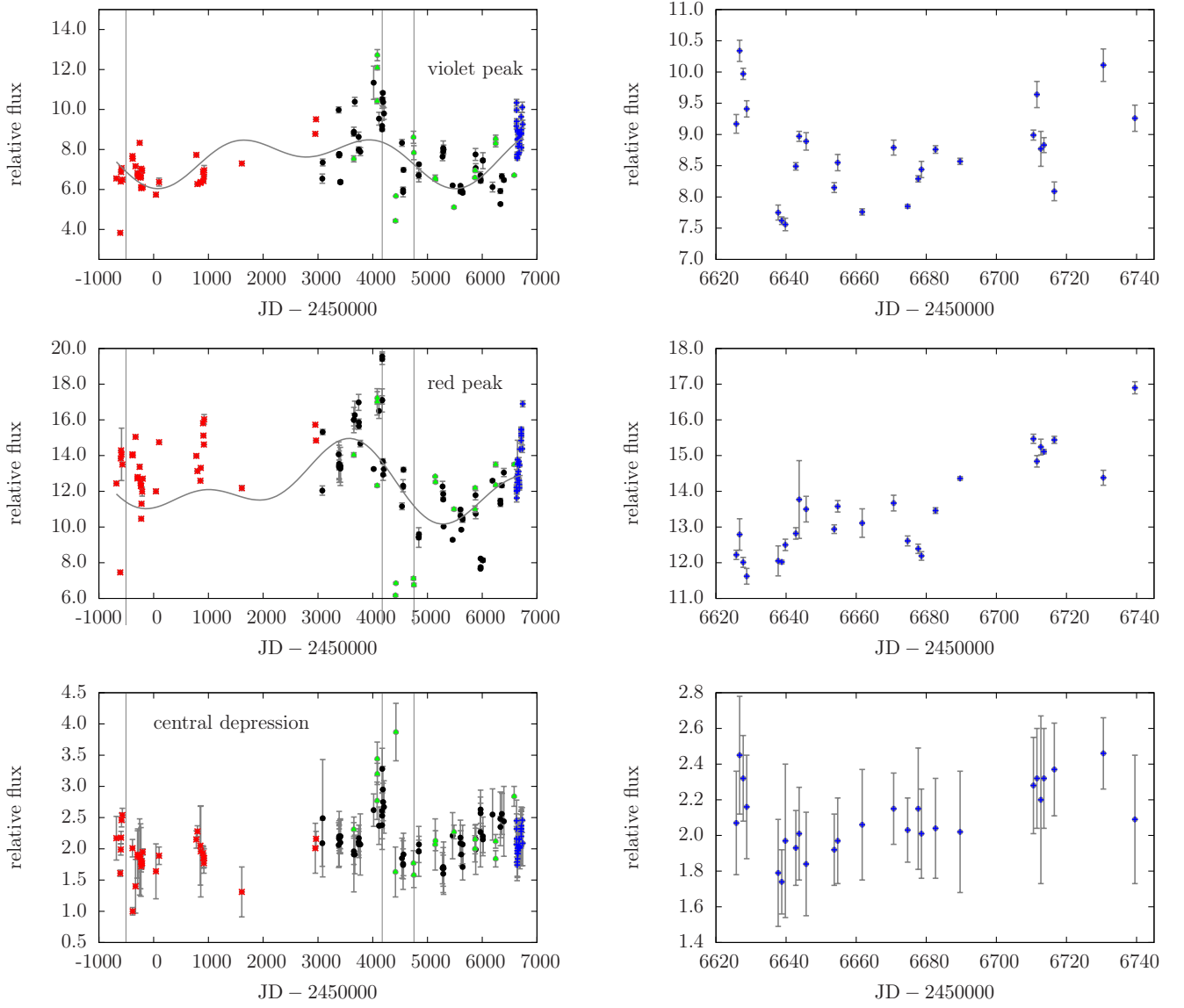


**Fig. 8.** Relative fluxes of violet and red peak (upper) and of the central depression of the H $\alpha$  line. The minimum and maximum value of  $|EW|$  of the H $\alpha$  line and its  $V/R > 1$  are shown by the vertical lines. The curve at two upper graphs is a fit of linear combinations of two sine functions with the fixed periods obtained from the period analysis of the H $\alpha$  EWs.

**Table 3.**  $V/R$  changes of the  $H\alpha$  line

date	$V/R$	Dispersion/ Resolution	Ref.
1981-Feb-01	0.65	5.5 Å/mm	1
1987-Feb-09	0.388 <sup>a</sup>	$R = 50\,000$	2
	0.384		
1987-Mar-22	0.6	$R = 7\,300$	3
1999-Oct-17	0.36	$R = 55\,000$	4
2007-Oct-04	0.88	$R = 55\,000$	4

**References.** (1) Andriolat & Fehrenbach (1982); (2) Dachs et al. (1992); (3) Halbedel (1991); (4) Borges Fernandes et al. (2009).

**Notes.** <sup>(a)</sup> double peak violet part with almost the same intensity

**Table 4.**  $EW$  of the  $H\alpha$  line

date	$EW$ (Å)	Dispersion/ Resolution	Ref.
1960-Feb-20	−116	12.4 Å/mm	1
1981-Feb-01	−47.2	5.5 Å/mm	2
1987-Feb-09	−50.1 ± 3	$R = 50\,000$	3
1987-Mar-22	−58.4	$R = 7\,300$	4
1994-Mar-15	−49.0	$R = 40\,000$	5
1994-Mar-16	−56.2	$R = 40\,000$	5
1995-Jan-11	−67 ± 4	$R = 5\,000$	6
1997-Jan-01	−58 ± 3	$R = 5\,000$	6
1999-Dec-18	−54 ± 3	$R = 8\,500$	7
2002-Jan-28	−71 ± 7	$R = 7\,500$	8
2002-Sep-20	−77 ± 7	$R = 15\,000$	8
1999-Oct-17	−61.35	$R = 55\,000$	9
2007-Oct-04	−57.56	$R = 55\,000$	9

**References.** (1) Doazan (1965); (2) Andriolat & Fehrenbach (1982); (3) Dachs et al. (1992); (4) Halbedel (1991); (5) Pogodin (1997); (6) Oudmaijer & Drew (1999); (7) Vink et al. (2002); (8) Baines et al. (2006); (9) Borges Fernandes et al. (2009).

**Table 5.**  $RV$ s of the  $H\alpha$ 

date	$RV$ (km s <sup>−1</sup> )	Dispersion/ Resolution	Ref.
$rv_{cd}$ 1960-Feb-20	57 ± 5	12.4 Å/mm	1
$rv_{cd}$ 1960-Feb-23	52 ± 5	12.4 Å/mm	1
$rv_{cd}$ 1967-Jan-27	50	9.7 Å/mm	2
$rv_{cd}$ 1987-Feb-09	−2 ± 2	$R = 50\,000$	3
$rv_{cd}$ 1987-Mar-22	61.4	$R = 7\,300$	4
$rv_{cd}$ 1995-Jan-11,	18	$R = 5\,000$	5
1997-Jan-01			
$rv_{cd}$ 1999-Oct-17	60	$R = 55\,000$	6
$rv_{cd}$ 2007-Oct-04	60	$R = 55\,000$	6
$rv_v$ 1987-Feb-09	−124 ± 2 <sup>b</sup>	$R = 50\,000$	3
	−50 ± 2		
$rv_r$ 1987-Feb-09	76 ± 2	$R = 50\,000$	3

**References.** (1) Doazan (1965); (2) Andriolat & Houziaux (1972); (3) Dachs et al. (1992); (4) Halbedel (1991); (5) Oudmaijer & Drew (1999); (6) Borges Fernandes et al. (2009).

**Notes.**  $rv_v$ ,  $rv_r$ ,  $rv_{cd}$   $RV$ s of the violet, red peak, and central depression; <sup>(b)</sup> double peak violet part with almost the same intensity

**Table 6.** Peak separation of the  $H\alpha$  line

date	Separation (km s <sup>−1</sup> )	Dispersion/ Resolution	Ref.
1995-Jan-11, 1997-Jan-01	160	$R = 5\,000$	1
1999-Oct-17	160	$R = 55\,000$	2
2007-Oct-04	150	$R = 55\,000$	2

**References.** (1) Oudmaijer & Drew (1999); (2) Borges Fernandes et al. (2009).

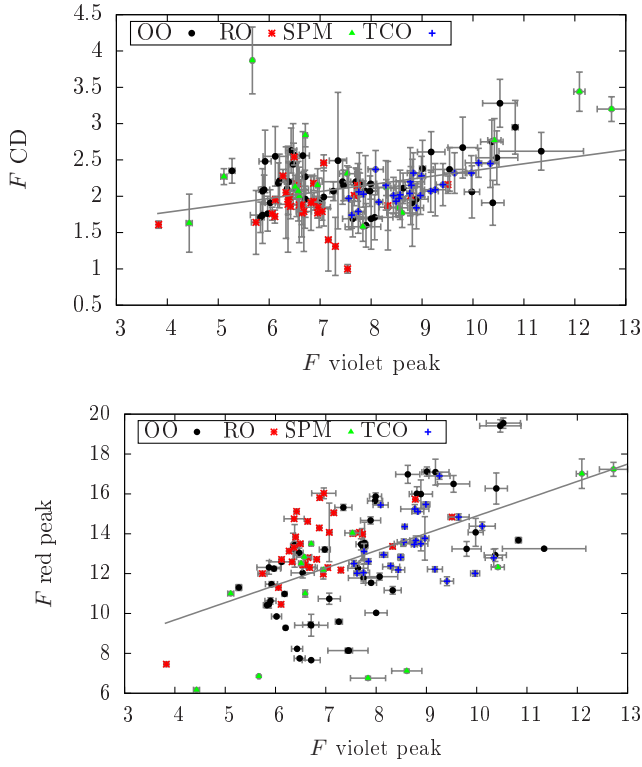


**Fig. 10.** Correlation between fluxes of H $\alpha$  line.

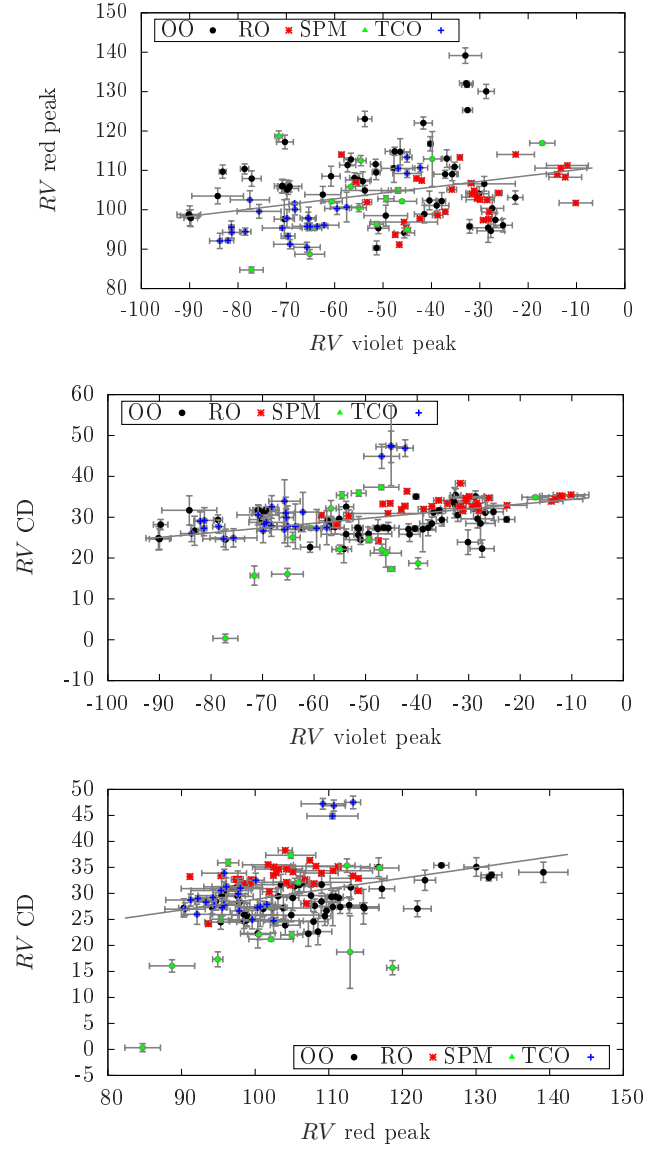


**Fig. 11.** Correlation between RV of H $\alpha$  line.

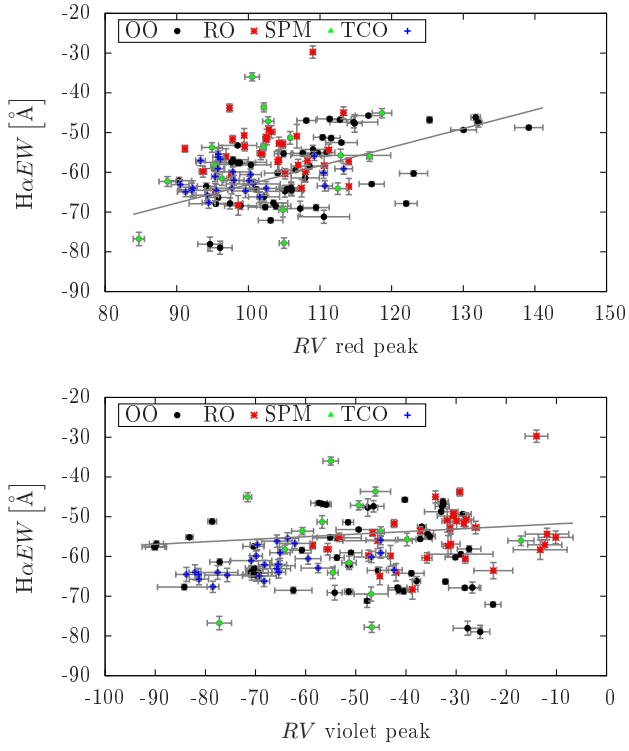


**Fig. 12.** Correlation between  $EW$  and  $RV$  of  $H\alpha$  line.



**Table 7.** Pearson correlation coefficients of the individual quantities of the H $\alpha$  line in different epochs.

JD	2449319– 2452110	2452110– 2454650	2454650– 2456600	2456600– 2456740	the entire sample
critical value	0.37	0.31	0.33	0.39	0.13
$P( EW , RV_W)$	0.09	-0.22	-0.07	0.69	-0.04
$P( EW , RV_{VP})$	-0.08	0.39	-0.28	-0.51	-0.22
$P( EW , F_{VP})$	-0.26	0.84	0.12	0.34	0.67
$P( EW , F_{CD})$	-0.21	0.32	0.23	0.51	0.38
$P( EW , F_{RP})$	-0.06	0.89	0.84	0.76	0.75
$P(RV_W, RV_{VP})$	0.13	-0.12	0.04	-0.51	-0.12
$P(RV_W, F_{RP})$	0.23	-0.42	0.02	0.65	0.15
$P(RV_{VP}, RV_{CD})$	0.68	0.23	0.37	0.82	0.38
$P(RV_{VP}, RV_{RP})$	0.32	-0.08	0.46	0.78	0.31
$P(RV_{VP}, F_{RP})$	-0.19	0.38	-0.42	-0.66	-0.07
$P(F_{VP}, RV_{RP})$	-0.18	0.02	-0.18	0.55	-0.22
$P(F_{VP}, F_{RP})$	0.62	0.62	0.07	0.22	0.54
$P(RV_{CD}, F_{VP})$	0.50	-0.14	0.40	0.28	-0.07
$P(RV_{CD}, RV_{RP})$	0.25	0.16	0.57	0.80	0.32
$P(RV_{RP}, F_{RP})$	0.01	-0.30	-0.48	-0.28	-0.47

**Notes.** The dependencies listed here were identified based on the value of Pearson coefficient, and also on the correlation diagrams. Notation:  $RV$  radial velocity,  $EW$  equivalent width,  $VP$  violet peak,  $RP$  red peak,  $CD$  central depression,  $W$  wings.

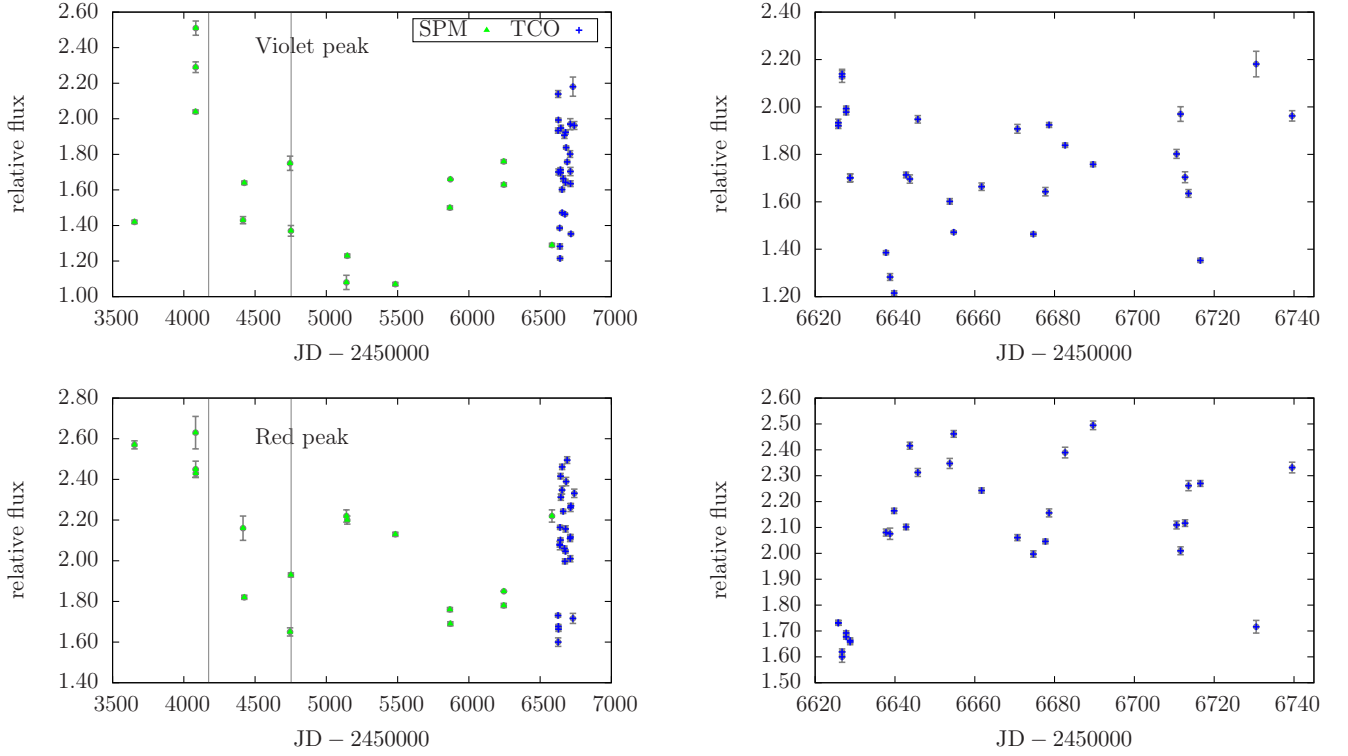


**Fig. 14.** Relative fluxes of the violet and red peaks of the spectral line H $\beta$ . Vertical lines show the maximum value of  $|EW|$  of the H $\alpha$  line and the epoch when  $V/R$  of the H $\alpha$  line was greater than one.

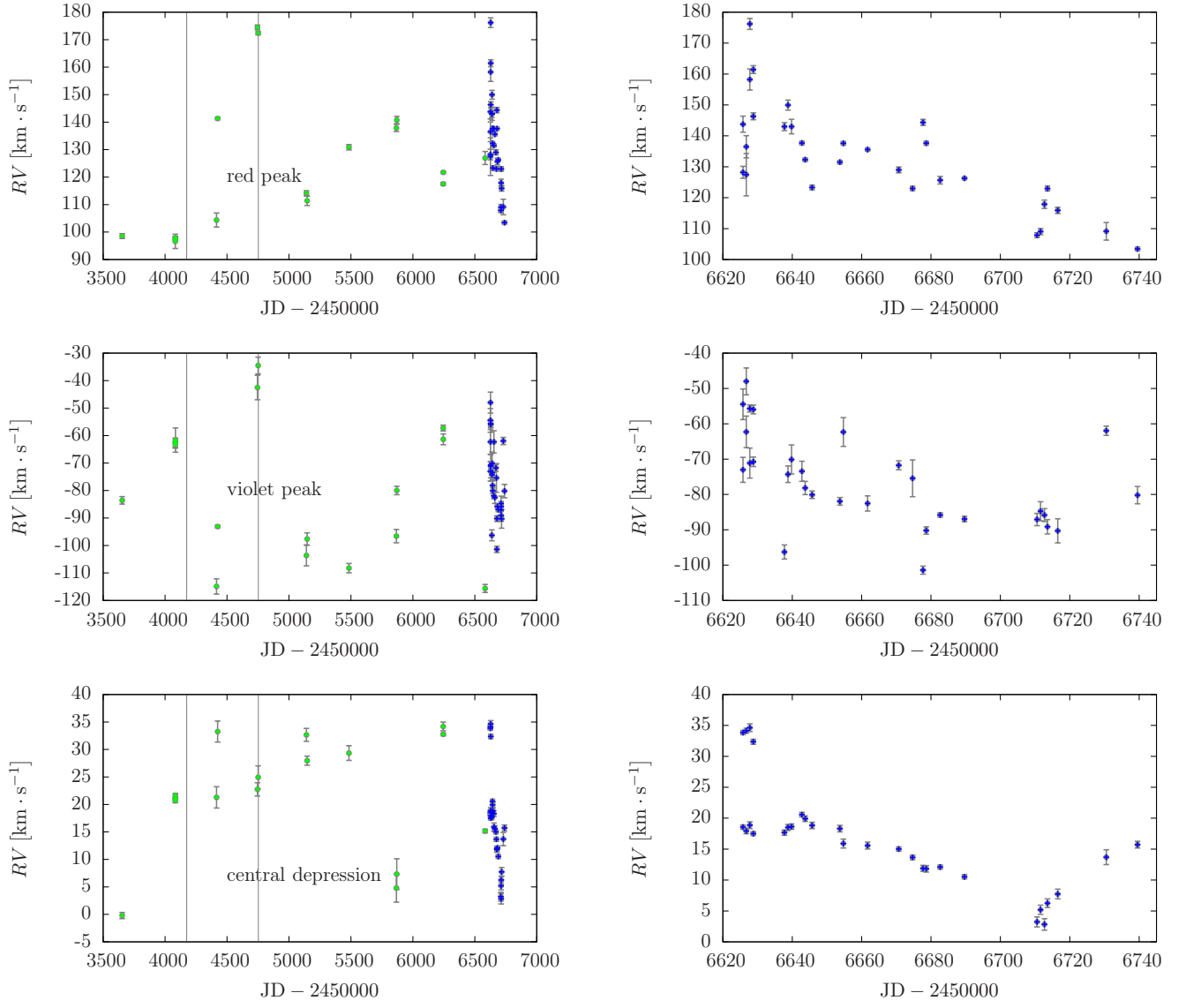


**Fig. 15.** RVs of the red peak, the violet peak, and the central depression of the H $\beta$  line.

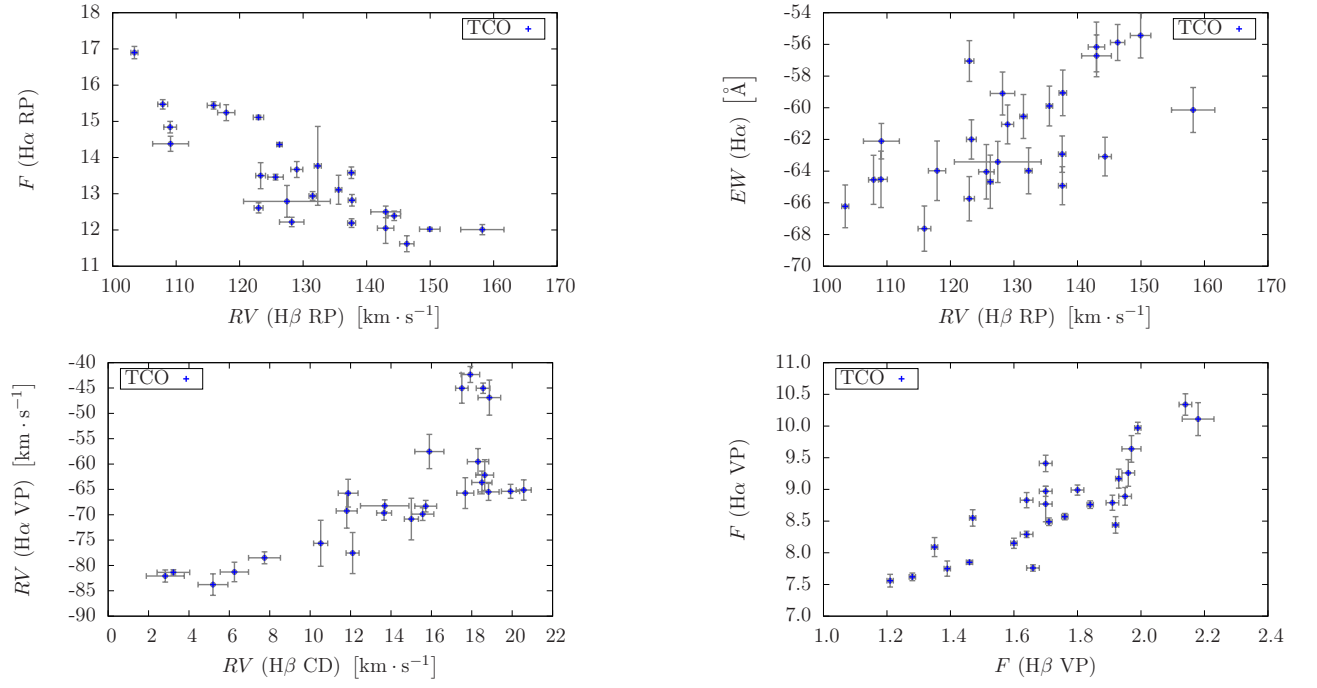


**Fig. 16.** Correlation diagrams of  $H\alpha$  and  $H\beta$  lines. Notation:  $RV$  radial velocity,  $EW$  equivalent width, VP violet peak, RP red peak, and CD central depression.

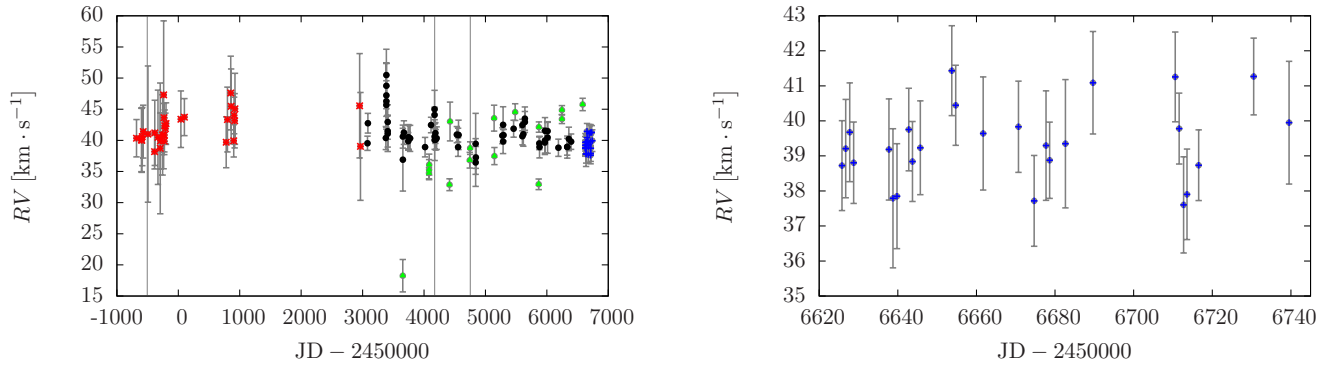


**Fig. 21.**  $RV$  of the [O I] 6364 Å line.

**Table 8.** *RVs of the oxygen lines*

line	date	RV (km s <sup>-1</sup> )	Dispersion/ Resolution	Ref.
[O I] 6300 Å	1945-Oct-24	36		1
[O I] 6300 Å	1960-Jan-03	34	12 Å/mm	2
[O I] 6364 Å	1960-Jan-03	44	12 Å/mm	2
[O I] 6300 Å	1970-Dec	22 ± 7	40 Å/mm	3
[O I] 6364 Å	1970-Dec	28 ± 7	40 Å/mm	3
[O I] 6364 Å	1995-Jan-11, 1997-Jan-01	33 ± 5	$R = 5\,000$	4
[O I] 6300 Å	1999-Oct-17	38.1	$R = 55\,000$	5
[O I] 6364 Å	1999-Oct-17	37.7	$R = 55\,000$	5
[O I] 6300 Å	2007-Oct-04	38.1	$R = 55\,000$	5
[O I] 6364 Å	2007-Oct-04	37.7	$R = 55\,000$	5

**References.** (1) Merrill (1952) (2) Houziaux (1960); (3) Andrillat & Houziaux (1972); (4) Oudmaijer & Drew (1999); (5) Borges Fernandes et al. (2009).

**Table 9.** *EWs of the oxygen lines*

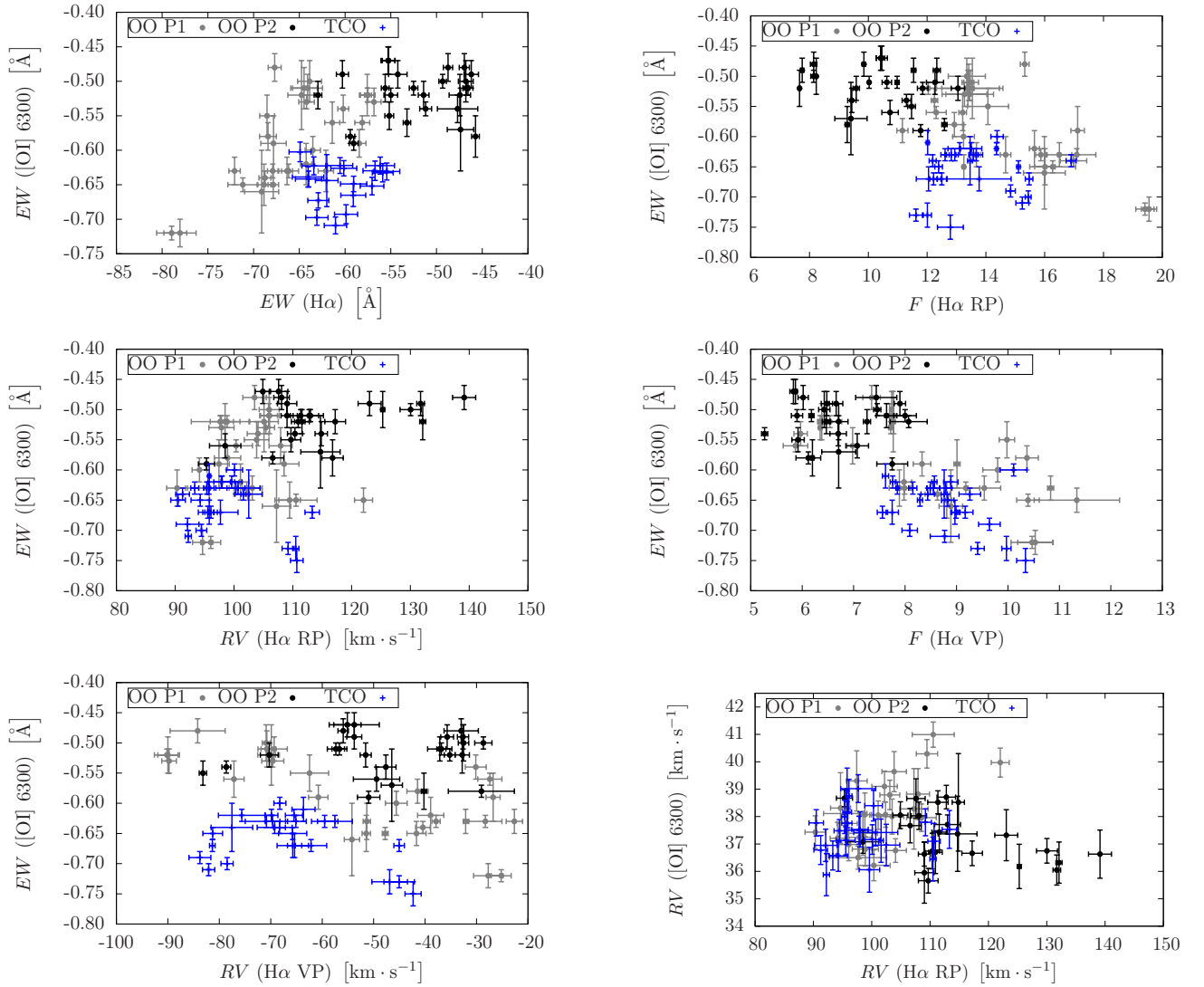
line	date	EW (Å)	Dispersion/ Resolution	Ref.
[O I] 6300 Å	1999-Oct-17	-0.55	$R = 55\,000$	1
[O I] 6300 Å	2007-Oct-04	-0.58	$R = 55\,000$	1
[O I] 6364 Å	1999-Oct-17	-0.20	$R = 55\,000$	1
[O I] 6364 Å	2007-Oct-04	-0.21	$R = 55\,000$	1

**References.** (1) Borges Fernandes et al. (2009).



**Table 10.** Correlation coefficients of the [O I] 6300 Å and H $\alpha$  lines in individual epochs.

JD	2453079– 2454650	2454650– 2456600	2456600– 2456740	the entire sample
$P(EW(H\alpha), EW([O I] \lambda 6300 \text{ Å}))$	0.70	0.11	0.06	0.56
critical value	0.35	0.38	0.37	0.22
$P(F(H\alpha RP), EW([O I] \lambda 6300 \text{ Å}))$	-0.70	-0.24	0.07	-0.57
critical value	0.35	0.38	0.37	0.22
$P(RV(H\alpha RP), EW([O I] \lambda 6300 \text{ Å}))$	0.08	0.39	0.40	0.49
critical value	0.35	0.38	0.37	0.22
$P(F(H\alpha VP), EW([O I] \lambda 6300 \text{ Å}))$	-0.70	-0.01	-0.44	-0.70
critical value	0.35	0.38	0.37	0.22
$P(RV(H\alpha VP), EW([O I] \lambda 6300 \text{ Å}))$	-0.73	0.10	-0.34	0.00
critical value	0.35	0.38	0.37	0.22
$P(RV(H\alpha RP), RV([O I] \lambda 6300 \text{ Å}))$	-0.61	0.57	-0.04	0.03
critical value	0.37	0.42	0.41	0.22

**Fig. 22.** Correlation diagram of H $\alpha$  and [O I]  $\lambda$  6300 Å lines. Dots consistently denote the measurements of spectra from Ondřejov observatory and crosses from TCO observatory throughout the paper. The values before the event, when  $V/R > 1$ , are in black. Blue indicates the value after another maximum in  $V/R$  changes. The epoch between is in grey. To emphasise that the same epochs are also defined by the RVs of the central depression, the error bars are coloured according to the RV extrema. The black, grey, and blue are used chronologically.

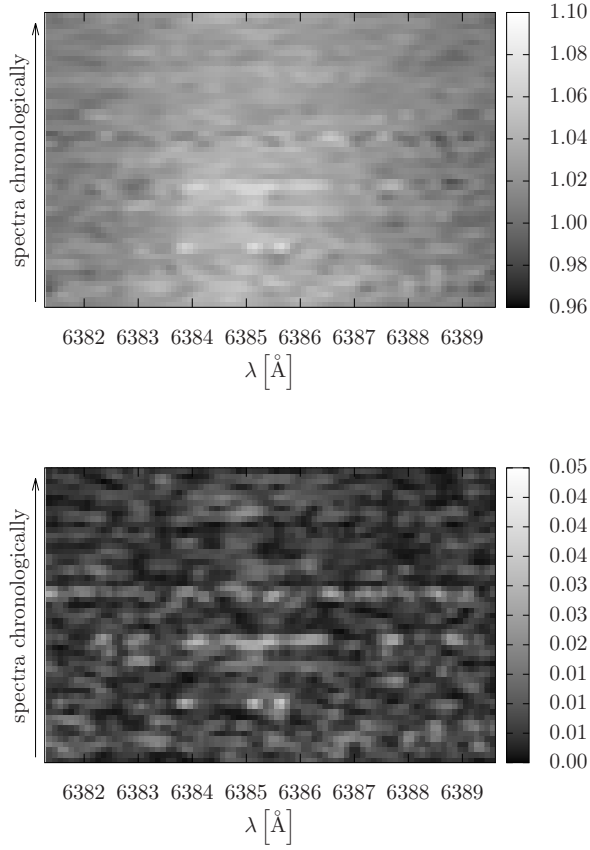


**Fig. 26.** Variability of Fe II 6384 Å line. *upper panel:* Grey-scale representation. *bottom panel:* Absolute variance from average.

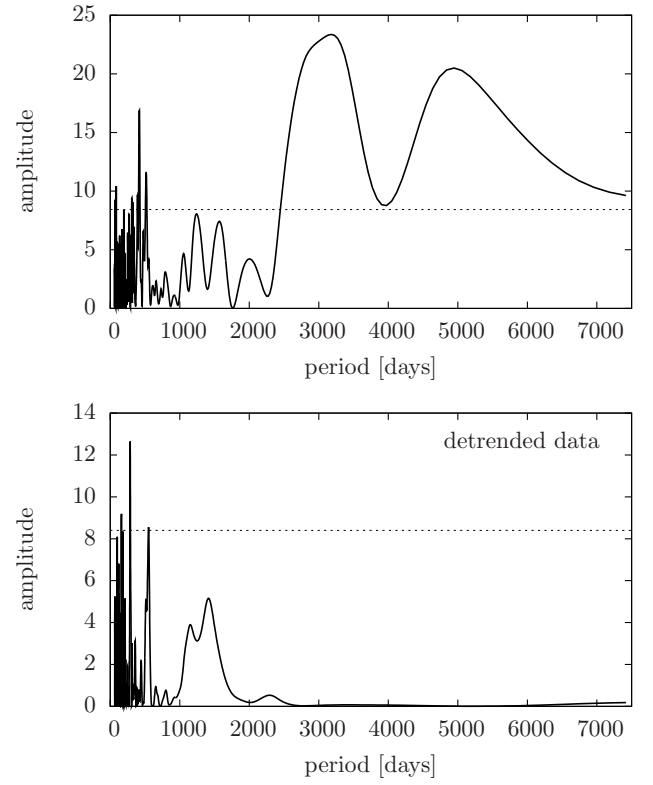


**Fig. 28.** Power spectra of the H $\alpha$  EWs. *upper panel:* Periodogram of the measured values of EWs. *bottom panel:* Periodogram after the removal of the long-term trends by the dynamical averaging.

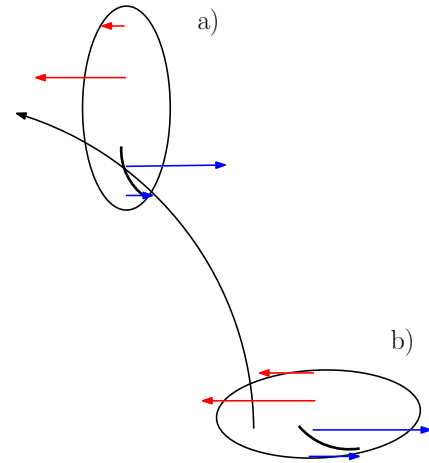


**Fig. 29.** Possible system geometry corresponding to H $\beta$   $V/R > 1$ . *a)* JD  $\sim 2454000$ :  $RV(H\alpha(RP))$  shows the local minimum,  $F(H\alpha(RP))$  maximum, and  $RV(H\alpha(VP))$  minimum; *b)* JD  $\sim 2454800$ :  $RV(H\alpha(RP))$  reaches the local maximum, and  $F(H\alpha(RP))$  minimum. The straightforward inclusion of other measured quantities is not possible. To determine them and prove the model, the radiative transfer based on hydrodynamic simulations is needed.